Available online at www.sciencedirect.com
SCIENCE DIRECT®
Icarus 174 (2005) 105–134
ICARUS
www.elsevier.com/locate/icarus

Evolution of a Keplerian disk of colliding and fragmenting particles: a kinetic model with application to the Edgeworth–Kuiper belt

Alexander V. Krivov *, Miodrag Sremčević, Frank Spahn

Nonlinear Dynamics Group, Institute of Physics, University of Potsdam, Am Neuen Palais 10, Bldg. 19, 14469 Potsdam, Germany

Received 4 June 2004; revised 28 September 2004

Abstract

We present a kinetic model of a disk of solid particles, orbiting a primary and experiencing inelastic collisions. In distinction to other collisional models that use a 2D (mass–semimajor axis) binning and perform a separate analysis of the velocity (eccentricity, inclination) evolution, we choose mass and orbital elements as independent variables of a phase space. The distribution function in this space contains full information on the combined mass, spatial, and velocity distributions of particles. A general kinetic equation for the distribution function is derived, valid for any set of orbital elements and for any collisional outcome, specified by a single kernel function. The first implementation of the model utilizes a 3D phase space (mass–semimajor axis–eccentricity) and involves averages over the inclination and all angular elements. We assume collisions to be destructive, simulate them with available material- and size-dependent scaling laws, and include collisional damping. A closed set of kinetic equations for a mass–semimajor axis–eccentricity distribution is written and transformation rules to usual mass and spatial distributions of the disk material are obtained. The kinetic "core" of our approach is generic. It is possible to add inclination as an additional phase space variable, to include cratering collisions and agglomeration, dynamical friction and viscous stirring, gravity of large perturbers, drag forces, and other effects into the model. As a specific application, we address the collisional evolution of the classical population in the Edgeworth–Kuiper belt (EKB). We run the model for different initial disk's masses and radial profiles and different impact strengths of objects. Our results for the size distribution, collisional timescales, and mass loss are in agreement with previous studies. In particular, collisional evolution is found to be most substantial in the inner part of the EKB, where the separation size between the survivors over EKB's age and fragments of earlier collisions lies between a few and several tens of km. The size distribution in the EKB is not a single Dohnanyi-type power law, reflecting the size dependence of the critical specific energy in both strength and gravity regimes. The net mass loss rate of an evolved disk is nearly constant and is dominated by disruption of larger objects. Finally, assuming an initially uniform distribution of orbital eccentricities, we show that an evolved disk contains more objects in orbits with intermediate eccentricities than in nearly circular or more eccentric orbits. This property holds for objects of any size and is explained in terms of collisional probabilities. The effect should modulate the eccentricity distribution shaped by dynamical mechanisms, such as resonances and truncation of perihelia by Neptune.

Keywords: Orbits; Collisional physics; Impact processes; Kuiper belt objects; Planetesimals

1. Introduction

Many astronomical objects can be classified as collisionally-evolving Keplerian disks. These include the solar nebula and protoplanetary disks of other stars, the Edgeworth–Kuiper disk, main asteroid belt, interplanetary dust cloud in the Solar System, circumstellar debris disks, planetary rings, and many others. The difference in mass, spatial, and time scales in all these systems is huge, as are differences in dynamical and physical processes that govern them. For instance, purely gravitational dynamics and predominantly catastrophic and cratering collisions in the asteroid belt can be contrasted to viscous, dissipative dynamics and agglomerating collisions in protoplanetary disks. Still, all these sys-

* Corresponding author. On leave from: Astronomical Institute, St. Petersburg University, Stary Peterhof, 198504 St. Petersburg, Russia.
E-mail address: krivov@agnld.uni-potsdam.de (A.V. Krivov).

0019-1035/$ – see front matter
doi:10.1016/j.icarus.2004.10.003

tems do have much in common. They all consist of solid particles orbiting a massive primary in orbits that can be approximated (at least adiabatically) with Keplerian ones. The particles experience frequent collisions which, depending on the masses, mechanical properties of colliders, as well as their relative velocities, can result either in full or partial disruption, restitution, or agglomeration of both particles. Collisions represent an important source as well as a sink for the disk material and reprocess mass, spatial, and velocity distributions of particles. Depending on the system, especially on the preponderant collisional outcomes, different types of collisional evolution may occur: growth of larger bodies (protoplanetary disks), gradual depletion of the disk (asteroids), and adiabatic steady-state (planetary rings).

The systems described above have been studied by a variety of methods. A straightforward, *N-body approach*—to follow dynamics of many individual objects and to perform true collision simulations—remains important for studying "difficult" cases where many other methods fail, such as the final stages of planet formation (e.g., Ida and Makino, 1993; Kokubo and Ida, 1998; Charnoz et al., 2001; Charnoz and Brahic, 2001). It can also be useful when the dynamics are complex, whereas any collisional event can be treated in a simple way (see Lecavelier des Etangs et al., 1996, for an application to debris disks). However, this method cannot treat more than $\sim 10^4$ objects and has an intrinsic problem in detecting collisions during the integration, which restricts its applicability. An alternative method is to replace particles themselves with their distribution in an appropriate phase space. Common methods are *smoothed particle hydrodynamics* (Monaghan, 1992) and *true hydrodynamics* (Lynden-Bell and Pringle, 1974; Pringle, 1981; Kley, 1999; Sremčević et al., 2002). Both deal with several lowest moments of the distributions and therefore are very efficient in describing formation of density structures due to diffusion effects or gravity of embedded perturbers, but are not suitable for collision-dominated systems. Finally, most general is the *kinetic method* of statistical physics (Boltzmann, 1896; Chapman and Cowling, 1970; Résibois and de Leener, 1977; Spahn et al., 2004) that considers the distribution functions themselves. The kinetic method can also be combined with the single-particle dynamics. For example, the state of the art in calculations of planetesimal evolution at the runaway growth stage is the so-called "two-groups approximation" (Weidenschilling et al., 1997; Goldreich et al., 2004) is which kinetic equations for numerous small planetesimals are solved together with N-body-type equations for a few large protoplanets.

In many astronomical problems, the kinetic method has been applied to derive a mass (or size) distribution and its evolution from the so-called coagulation equation, or Smoluchowski equation (Smoluchowski, 1916; Chandrasekhar, 1943). Note that the term "coagulation equation" is actually used regardless of whether the colliding particles merge, fragment, or just change their velocities. In particular cases when the coalescence (or fragmentation) coefficient is constant or depends on masses in a simple way, analytic solutions have been found (see Safronov, 1969; Dohnanyi, 1969; Dorschner, 1970; Silk and Takahashi, 1979; Wetherill, 1990, and references therein). Otherwise, the equation is integrated numerically. The coagulation equation alone is sufficient to describe diffuse media, for instance growth of dust grains in the interstellar space (Oort and van de Hulst, 1946) and fragmentation of collapsing molecular clouds (Silk and Takahashi, 1979).

In any disk system, however, the spatial extent of the system makes collisional rates among the bodies and their relative velocities dependent on the distance from the primary. A classical technique originally proposed to study the evolution of a planetesimal swarm (e.g., Greenberg et al., 1978; Wetherill, 1990) is to approximate the disk with a set of concentric semimajor axis annuli and a set of mass batches in each of those. Every semimajor axis zone is then treated with a particle-in-a-box method: to quantify random velocities between the particles in a given semimajor axis zone, one introduces mean values of eccentricity $\langle e \rangle$ and inclination $\langle i \rangle$, pre-calculates collisional rates, and then solves the coagulation-type equation for the mass distribution. Both $\langle e \rangle$ and $\langle i \rangle$ are constant input parameters, which may or may not be different for different mass bins and spatial annuli. Models of this type were developed and applied to the accumulation of planetesimals (Greenberg et al., 1978; Nakagawa et al., 1983; Wetherill and Stewart, 1989), collisional evolution of asteroids (e.g., Campo Bagatin et al., 1994; Davis and Farinella, 1997) and Edgeworth–Kuiper belt (EKB) objects (e.g., Stern, 1995, 1996; Stern and Colwell, 1997; Durda and Stern, 2000), and for circumstellar debris disks (e.g., Krivov et al., 2000; Dominik and Decin, 2003; Thébault et al., 2003).

To achieve a reasonable degree of fidelity, especially for systems that are very sensitive to velocities (evolution of protoplanetary disks and formation of planets), the evolution of the mass distribution must be considered simultaneously with the velocity evolution (see, e.g., Lissauer and Stewart, 1993, for a review). Equations for the random velocities or equivalently, for $\langle e \rangle$ and $\langle i \rangle$ may include modification of velocities by physical collisions, dynamical friction, viscous stirring, etc. (see, e.g., Wetherill and Stewart, 1993; Stewart and Ida, 2000, and references therein). Taken alone, these equations can already be useful in some applications. For example, in the theory of dense planetary rings where direct N-body simulations and hydrodynamics are preferred methods, the Boltzmann-type kinetic equations for velocity have been used to study the vertical structure of the rings (Frezzotti, 2001). A more common approach, however, is to integrate the velocity equations simultaneously with the coagulation equation for the mass distribution. Another substantial improvement recently made to the models was to use multiannulus codes, in which the particles belonging to different semimajor axis zones can collide and produce fragments that may go into other zones (Spaute et al., 1991; Weidenschilling et al., 1997). Multiannulus models taking full account of the velocity evolution may also include a multitude of additional effects, such as gas drag, Poynting–Robertson drag, and gravitational perturbations by massive objects (Kenyon and Luu, 1998, 1999a, 1999b; Kenyon and Bromley, 2002, 2004a, 2004b).

All these methods, being very powerful and providing accurate results, are "hybrid" in the sense that they consider the velocity evolution and orbital dynamics, separately from the mass and/or spatial distribution of the material. An indication for that is that all of these approaches consider two groups of equations, one for the masses and semimajor axes, and another one for the eccentricities and inclinations (or the velocity components). In this paper, we propose a different version of the kinetic approach, which relies on the simple idea that orbital elements of the disk particles contain full information on their position and velocity. We thus consider mass and orbital elements of the particles as independent, and equally important, variables and systematically formulate all parts of the theory, including the coagulation equation, equations for collisional rates and the velocity evolution equations, in terms of these variables. This results in a single set of kinetic equations with respect to one mathematical object, a phase space distribution $n(m$, orbital elements). Moreover, the equations are written in a covariant form, allowing one to choose orbital elements in a flexible way (Keplerian elements, Delaunay variables etc.) and to reduce the number of degrees of freedom (e.g., by using averaging over some of the elements). The first implementation of the model presented here uses a 3-dimensional phase space, comprising the particle mass m, orbital semimajor axis a, and eccentricity e and involving averages over the inclination i and all angular elements. A new version of the model with a (m, a, e, i)-phase space will follow.

We believe that this approach is simpler conceptually than the methods outlined above. It automatically enables a study of the simultaneous evolution of mass, spatial, and velocity distribution of particles. It does not involve any separation between the arguments of $n(m, a, e, i, \ldots)$, which makes the method ideal for detection of possible combined effects. Further, it does not assume an a priori functional form of the distribution of orbital elements (for instance, a uniform distribution in eccentricities as in Spaute et al. (1991); Weidenschilling et al. (1997)), which has a bonus for dynamically hot disks with broad ranges of semimajor axes and orbital eccentricities. A multiannulus treatment is an intrinsic property of our approach. Of course, our method is not free of disadvantages. Particular physical effects one may wish to incorporate have to be described in terms of orbital elements, which would require additional effort. Also, the model is more demanding with respect to computing resources, because it deals with a multidimensional phase space.

To render the problem tractable, we are forced to make many simplifying assumptions. It is important, however, to distinguish between principal limitations and those that can be lifted without changing the conceptual "core" of our approach. The assumptions of the first kind are as follows: (i) the system is not too dense to ensure that finite-size effects are absent, the packing factor is negligible, triple and multiple collisions are unimportant etc.; (ii) no energy is partitioned into rotational degrees of freedom of the objects; (iii) the largest bodies considered are still numerous enough to be represented by a continuous distribution, which is a principal limitation inherent to the coagulation equation (Tanaka and Nakazawa, 1994).

We now list the assumptions of the second kind: (1) the inclination distribution does not evolve with time; (2) apsides and nodes of particles' orbits are distributed uniformly and therefore, the disk is rotationally symmetric; (3) between collisions, all particles move in Keplerian orbits; (4) these orbits are bound, i.e., elliptic; (5) long-range interactions (dynamical friction, viscous stirring, distant perturbations etc.) are absent; (6) any collision with a sufficiently high impact energy leads to full destruction of both colliders and generation of smaller debris; (7) there is no direct supply of material into the system. Assumptions (1)–(2) can, in principle, be lifted by adding inclination and/or angular elements to the list of phase space variables and by treating them in the same way as semimajor axis and eccentricity. This step is straightforward as far as derivation of formulas is concerned, but would result in a model very demanding to the computer resources. We estimate that adding one more variable, but no more, would still yield a model that delivers results in reasonable time. In contrast, lifting assumptions (3)–(7) would require additional effort, but would not pose any severe computational limitations. It should be possible to include radiation pressure and drag forces, or add a population of hyperbolic particles, include coagulation and restitution regime, or add distant interactions and supply terms. Thus our approach is generic enough and can potentially serve as a basis for, say, a planetary accretion code or a code for modeling dilute circumstellar debris disks with Poynting–Robertson transport and radiation pressure removal of small dust grains.

In Section 2, we introduce basic variables and distribution functions. In Section 3, integro-differential kinetic equations for the phase space distribution are derived. Section 4 discusses probabilistic and kinematic terms in the kinetic equations. In Section 5, the model of a single impact event is compiled. Section 6 applies the model to the collisional evolution of the EKB. Section 7 contains a summary and discusses possible extensions of the model. Appendix A presents a numerical method for solving the kinetic equations and its computer implementation. Appendix B provides an explanation of a new effect in the combined (e, a)-distribution of a collisionally evolving disk.

2. Distribution functions

The system considered here is a disk of "particles" moving in Keplerian orbits around a primary and experiencing destructive collisions. By "particles" we mean solids that are large enough not to be affected by non-gravitational forces, such as radiation pressure. This sets the lower bound on the particle sizes to ~ 1 mm. The upper bound is limited by the requirement (iii) in the Introduction and may be as large as hundreds of kilometers for systems like the EKB. In this section, we consider variables that characterize a particle's state and distribution functions that describe the ensemble of particles. The assumption (i) in the Introduction implies that we use the so-called single-particle distribution to describe the ensemble, meaning that each distribution function will have state variables of only one particle in its argument list.

2.1. Configuration space

Apart from masses of particles m, their radius vectors $\mathbf{r}$ and velocities $\mathbf{v}$ are the most natural state variables one can use to describe collisional processes. For instance, a condition that two particles collide is just the coincidence of their radius vectors: $\mathbf{r}_1 = \mathbf{r}_2$. The results are also best understood in terms of these variables. For example, the number density of particles or the surface mass density at a certain distance from the primary are usual quantities of interest. Unfortunately, in terms of coordinates and velocities, it is not easy to get rid of unnecessary degrees of freedom and to use natural symmetries of the problem. Below we shall see that this can be easily done by using orbital elements.

2.2. Orbital element space

The orbit of each particle in the disk may be described by six Keplerian elements: the semimajor axis a, eccentricity e, inclination i, longitude of the ascending node Ω, argument of pericenter ω, and the mean anomaly M. We assume a rotationally symmetric disk with semi-opening angle ε (Fig. 1). This implies that the distribution of both Ω and ω is uniform, and that $0 \leqslant i \leqslant \varepsilon$. We will also assume that each orbit is densely populated by particles, so that the fast variable—mean anomaly M—has a uniform distribution as well. Denote by $\mathbf{p} \equiv (a, e, i)$ the three positional elements and by $\mathbf{q} \equiv (\Omega, \omega, M)$ the three angular elements. Dimension: $[\mathbf{p}] = [a][e][i] =$ cm, $[\mathbf{q}] = [\Omega][\omega][M] = 1$. The angular elements $\mathbf{q}$ will be eventually averaged out and will not appear in the final equations.

2.3. Notation conventions

(1) Below we will introduce several distribution functions, which will be denoted by one and the same letter n with different lists of arguments. These are treated as *different* functions. The quantity $n(x, y, \ldots)$ always has the following meaning: $n(x, y, \ldots)\,dx\,dy \ldots$ is the total number of particles in the disk with arguments $[x, x+dx]$, $[y, y+dy]$, …. Integration of $n(x, y, \ldots)$ over some of its arguments gives again a function n without those arguments. The quantity n without arguments is simply the total number of particles in the disk:

$$\int_x \int_y \ldots n(x, y, \ldots)\,dx\,dy \ldots = n. \tag{2.1}$$

(2) We will also use distribution functions denoted by $\varphi(\ldots)$. In contrast to $n(\ldots)$, these have a unit normalization:

$$\int_x \int_y \ldots \varphi(x, y, \ldots)\,dx\,dy \ldots = 1. \tag{2.2}$$

Obviously, each n-distribution with several arguments is a product of the n-distribution with a subset of arguments and the φ-distribution of the remaining arguments. Each φ-distribution with several arguments is a product of φ-distributions with subsets of arguments. For instance,

$$\begin{aligned} n(x, y, z) &= n\varphi(x, y, z) = n(x)\varphi(y, z) = n(x)\varphi(y)\varphi(z) \\ &= n(x, y)\varphi(z) \quad \text{etc.} \end{aligned} \tag{2.3}$$

Of course, these rules can only be applied if the distributions are independent.

(3) The quantity N stands for the number density of particles, i.e., for the number of particles per unit spatial volume. The exact meaning of N with different arguments is given below.

(4) The distributions $n(\ldots)$, $\varphi(\ldots)$, and $N(\ldots)$ are functions of time. For brevity, the argument t will be omitted (but is always implied). When defining each function, we indicate its dimension and show how the total number of particles in the disk can be expressed through that function.

2.4. Distributions in orbital element space

2.4.1. Phase space distribution function $n(m, \mathbf{p}, \mathbf{q})$

Central to our treatment is the distribution function $n(m, \mathbf{p}, \mathbf{q})$ so that $n(m, \mathbf{p}, \mathbf{q})\,dm\,d\mathbf{p}\,d\mathbf{q}$ is the number of particles with $[m, m+dm]$, $[\mathbf{p}, \mathbf{p}+d\mathbf{p}]$, $[\mathbf{q}, \mathbf{q}+d\mathbf{q}]$ (at a certain instant of time t). Dimension: $[n(m, \mathbf{p}, \mathbf{q})] = \mathrm{g}^{-1}\,\mathrm{cm}^{-1}$. The total number of particles in the disk is

$$n = \int_m \int_{\mathbf{p}} \int_{\mathbf{q}} n(m, \mathbf{p}, \mathbf{q})\,dm\,d\mathbf{p}\,d\mathbf{q}. \tag{2.4}$$

2.4.2. Averaged phase space distribution function $n(m, \mathbf{p})$

Another important quantity is a distribution function $n(m, \mathbf{p})$ integrated over the angles:

$$n(m, \mathbf{p}) = \int_{\mathbf{q}} n(m, \mathbf{p}, \mathbf{q})\,d\mathbf{q}, \tag{2.5}$$

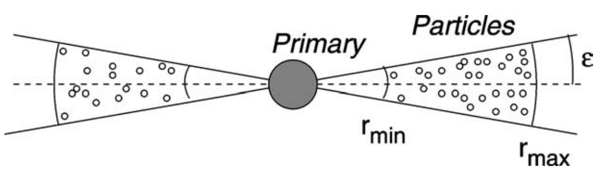

Fig. 1. Geometry of the disk seen edge-on.

with the dimension $[n(m, \mathbf{p})] = \mathrm{g}^{-1}\,\mathrm{cm}^{-1}$. The total number of particles in the disk is

$$n = \int_m \int_{\mathbf{p}} n(m, \mathbf{p})\, dm\, d\mathbf{p}. \tag{2.6}$$

We assume a uniform distribution of the lines of apsides and nodes:

$$n(m, \mathbf{p}, \mathbf{q}) = n(m, \mathbf{p})\varphi(\mathbf{q}) = n(m, \mathbf{p})\varphi(\Omega)\varphi(\omega)\varphi(M) \tag{2.7}$$

with

$$\varphi(\Omega) = \varphi(\omega) = \varphi(M) = 1/(2\pi) = \mathrm{const.} \tag{2.8}$$

2.5. *Distributions in configuration space*

2.5.1. *Mass-coordinate-velocity distribution function $n(m, \mathbf{r}, \mathbf{v})$*

The transformation between $(\mathbf{r}, \mathbf{v})$ and $(\mathbf{p}, \mathbf{q})$ is

$$d\mathbf{r}\, d\mathbf{v} \equiv J\, d\mathbf{p}\, d\mathbf{q}, \tag{2.9}$$

with the jacobian

$$J \equiv \left\| \frac{\partial(\mathbf{r}, \mathbf{v})}{\partial(\mathbf{p}, \mathbf{q})} \right\| = \frac{1}{2}\sqrt{(G\mathcal{M})^3 a}\, e \sin i, \tag{2.10}$$

where $\mathcal{M}$ is the mass of the primary, giving

$$n(m, \mathbf{r}, \mathbf{v}) = n(m, \mathbf{p}, \mathbf{q})J^{-1} = n(m, \mathbf{p})\varphi(\mathbf{q})J^{-1}. \tag{2.11}$$

In subsequent sections we will derive an equation for $n(m, \mathbf{p})$. Once it is solved, Eq. (2.11) can be used to calculate the distribution in terms of coordinates and velocities.

2.5.2. *Number density as a function of mass and coordinates $N(m, \mathbf{r})$*

The mass-spatial distribution can be characterized by $N(m, \mathbf{r})$, the number density of particles with masses $[m, m + dm]$ at the point $\mathbf{r} \equiv (r, \phi, \lambda)$, where ϕ is the "latitude" and λ is the "longitude." Dimension: $[N(m, r, \phi, \lambda)] = \mathrm{g}^{-1}\,\mathrm{cm}^{-3}$. The total number of particles in the disk is

$$n = \int_m dm \int_r \int_{-\pi/2}^{\pi/2} \int_0^{2\pi} N(m, r, \phi, \lambda) r^2\, dr \cos\phi\, d\phi\, d\lambda. \tag{2.12}$$

The function $N(m, \mathbf{r})$ can be found by integrating Eq. (2.11) over velocities. The result is a classical Haug's (1958) integral

$$N(m, r, \phi, \lambda) = \frac{1}{2\pi^3 r^3} \int_a \int_e \int_i n(m, a, e, i)\left(\frac{r}{a}\right)^{3/2} \times \left[2 - \frac{r}{a} - \frac{a}{r}(1 - e^2)\right]^{-1/2} \times \frac{1}{\sqrt{\cos^2\phi - \cos^2 i}}\, da\, de\, di, \tag{2.13}$$

where the integration domain is

$$a(1 - e) \leqslant r \leqslant a(1 + e), \qquad \cos^2 i \leqslant \cos^2\phi. \tag{2.14}$$

2.5.3. *Number density as a function of mass and distance $N(m, r)$*

We define the function $N(m, r)$ to be the vertically-averaged number density of particles with masses $[m, m + dm]$ at the point r:

$$N(m, r) \equiv \frac{\int_{-\varepsilon}^{\varepsilon} \int_0^{2\pi} N(m, r, \phi, \lambda) \cos\phi\, d\phi\, d\lambda}{\int_{-\varepsilon}^{\varepsilon} \int_0^{2\pi} \cos\phi\, d\phi\, d\lambda}. \tag{2.15}$$

Dimension: $[N(m, r)] = \mathrm{g}^{-1}\,\mathrm{cm}^{-3}$. The total number of particles in the disk is

$$n = \int_m dm \int_r \int_{-\varepsilon}^{\varepsilon} \int_0^{2\pi} N(m, r) r^2\, dr \cos\phi\, d\phi\, d\lambda. \tag{2.16}$$

In most of the applications, the distribution of inclinations can be assumed independent of the distribution of a, e: $n(m, a, e, i) = n(m, a, e)\varphi(i)$, where the distribution of inclinations is non-zero within $[0, \varepsilon]$ and is normalized to unity:

$$\int_0^{\varepsilon} \varphi(i)\, di = 1. \tag{2.17}$$

Then, inserting (2.13) into (2.15) leads to:

$$N(m, r) = \frac{1}{4\pi^2 \sin\varepsilon} \frac{1}{r^3} \iint n(m, a, e)\left(\frac{r}{a}\right)^{3/2} \times \left[2 - \frac{r}{a} - \frac{a}{r}(1 - e^2)\right]^{-1/2} da\, de, \tag{2.18}$$

where the integration domain is (see Fig. 2)

$$a(1 - e) \leqslant r \leqslant a(1 + e). \tag{2.19}$$

Equation (2.18) holds for any distribution of inclinations $\varphi(i)$ within $[0, \varepsilon]$—in particular, for a uniform distribution

$$\varphi(i) = \frac{\sin i}{1 - \cos\varepsilon}. \tag{2.20}$$

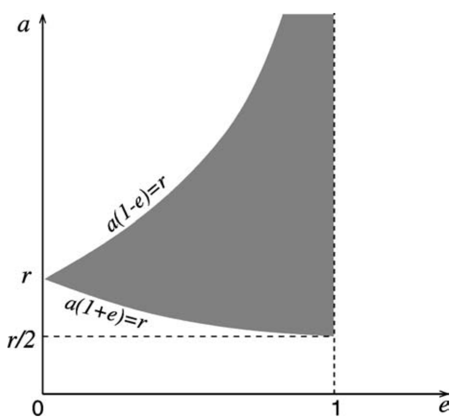

Fig. 2. Integration domain for Eq. (2.18) in the (e, a)-plane. The filled area corresponds to particles that contribute to the number density at a distance r.

Note that Eq. (2.18) has an integrable singularity at one of the borders of the integration domain, namely at the "pericentric" curve $a(1-e)=r$. This fact should be taken into account in the numerical implementation. Another potential difficulty in the numerical evaluation of the integral (2.18) is a curtailment of the integration domain for small values of e, i.e., for near-circular orbits, which is typically a densely populated part of the phase space. One can cope with the problem by applying the transformation of variables $(a,e)\to(\chi,e)$, where

$$a(\chi,e,r)=r\frac{1-e+2e\chi}{1-e^2} \tag{2.21}$$

which replaces Eq. (2.18) by

$$N(m,r)=\frac{1}{4\pi^2\sin\varepsilon}\frac{1}{r^2}\int_0^1\int_0^1 n\bigl(m,a(\chi,e,r),e\bigr) \times(1-e+2e\chi)^{-1}\sqrt{\frac{1-e^2}{\chi(1-\chi)}}\,d\chi\,de, \tag{2.22}$$

where the integration domain is a unit rectangle and $\chi=0$ and $\chi=1$ are integrable singularities.

2.5.4. Disk's parameters as functions of distance

Having calculated the vertically-averaged number density $N(m,r)$ as a function of mass and distance, one can easily obtain a number of other quantities of interest. Different authors use distributions of different physical quantities (e.g., number density, cross section density, mass density) with different arguments (particle mass or size) and of different type (differential, cumulative, per unit logarithmic size bin, etc.). In this paper, two specific distributions will be used: mass density per unit logarithmic size interval (size decade),

$$N_{m,10,s}(s,r)=3(\ln 10)m^2(s)N\bigl(m(s),r\bigr) \tag{2.23}$$

(s is the radius of a particle), and surface mass density

$$\Sigma(r)=2r\sin\epsilon\int mN(m,r)\,dm. \tag{2.24}$$

3. The kinetic equation

In this section, we derive integro-differential equations for the averaged phase space distribution function $n(m,\mathbf{p})$. We start with the kinetic equation in standard form, then rewrite it in terms of orbital elements, and finally average over some of the elements to make use of symmetries and to reduce computational complexity of the problem.

3.1. The kinetic equation in coordinates and velocities

Neglecting transport mechanisms such as drag forces, the time evolution of the phase space distribution function in terms of coordinates and velocities is given by an obvious master equation

$$\frac{dn}{dt}(m,\mathbf{r},\mathbf{v})=\left(\frac{dn}{dt}\right)_{\text{gain}}(m,\mathbf{r},\mathbf{v})-\left(\frac{dn}{dt}\right)_{\text{loss}}(m,\mathbf{r},\mathbf{v}). \tag{3.1}$$

Assume now that there are no physical sources and sinks of the material in the system, other than mutual collisions that eliminate the original particles (loss) and simultaneously create collisional fragments (gain). Then the terms in the right-hand side of Eq. (3.1) can be found by "counting" the particles destroyed and generated per unit time in a unit volume at a position $\mathbf{r}$ (Spahn et al., 2004):

$$\left(\frac{dn}{dt}\right)_{\text{gain}}(m,\mathbf{r},\mathbf{v})=\int\cdots\int_{m_p,\mathbf{v}_p;m_t,\mathbf{v}_t} F(\mathbf{r};m_p,\mathbf{v}_p;m_t,\mathbf{v}_t;m,\mathbf{v}) \times n(m_p,\mathbf{r},\mathbf{v}_p)n(m_t,\mathbf{r},\mathbf{v}_t) \times v_{\text{imp}}(\mathbf{r},\mathbf{v}_p,\mathbf{v}_t)\sigma(m_p,m_t) \times dm_p\,d\mathbf{v}_p\,dm_t\,d\mathbf{v}_t, \tag{3.2}$$

$$\left(\frac{dn}{dt}\right)_{\text{loss}}(m,\mathbf{r},\mathbf{v})=n(m,\mathbf{r},\mathbf{v})\iint_{m_p,\mathbf{v}_p} n(m_p,\mathbf{r},\mathbf{v}_p) \times v_{\text{imp}}(\mathbf{r},\mathbf{v}_p,\mathbf{v})\sigma(m_p,m)\,dm_p\,d\mathbf{v}_p. \tag{3.3}$$

Hereafter subscripts p and t refer to a projectile and a target particle, and we assume that these are the smaller and larger of the two colliders, respectively: $m_p\leqslant m_t$. Other quantities in Eqs. (3.1)–(3.3) are: σ is the collisional cross section: $\sigma(m_p,m_t)=\pi(s_p^2+s_t^2)$, where s is the radius of a particle; $\mathbf{v}_{\text{imp}}(\mathbf{r},\mathbf{v}_p,\mathbf{v}_t)\equiv\mathbf{v}_p(\mathbf{r})-\mathbf{v}_t(\mathbf{r})$ is the relative velocity of two particles colliding at the point $\mathbf{r}$. The function $F(\mathbf{r};m_p,\mathbf{v}_p;m_t,\mathbf{v}_t;m,\mathbf{v})$ that appears in the gain term describes the outcome of a binary collision: $F(\ldots)\,dm\,d\mathbf{v}$ is the number of fragments with $[m,m+dm]$, $[\mathbf{v},\mathbf{v}+d\mathbf{v}]$, produced by a collision of particles with $(m_p,\mathbf{v}_p)$ and $(m_t,\mathbf{v}_t)$ at the point $\mathbf{r}$. Dimension: $[F(\mathbf{r};m_p,\mathbf{v}_p;m_t,\mathbf{v}_t;m,\mathbf{v})]=\text{g}^{-1}\,\text{s}^3\,\text{cm}^{-3}$.

In the particular case when n and other functions in the integrands are independent of the velocities, Eqs. (3.1)–(3.3) reduce to the Smoluchowski equation. Similarly, when the masses are absent, Eqs. (3.1)–(3.3) transform to the Boltzmann equation. In that case, if the kernel F describes elastic collisions, the equation takes the form originally obtained by Boltzmann (1896).

3.2. Derivation of the kinetic equation in orbital elements

The kinetic equations (3.1)–(3.3) will be expressed in terms of the orbital elements. According to (2.11), the left-hand side of Eq. (3.1) transforms in a straightforward way:

$$\frac{dn}{dt}(m,\mathbf{r},\mathbf{v})=\frac{dn}{dt}(m,\mathbf{p},\mathbf{q})J^{-1}, \tag{3.4}$$

where the jacobian J is given by (2.10).

We now consider the gain term (3.2). Using the identity

$$G(\mathbf{r}, \mathbf{v}) = \int G(\mathbf{r}', \mathbf{v})\delta(\mathbf{r} - \mathbf{r}')\, d\mathbf{r}', \tag{3.5}$$

valid for any function G, results in

$$\begin{aligned}\left(\frac{dn}{dt}\right)_{\text{gain}}(m, \mathbf{r}, \mathbf{v}) &= \int\limits_{m_p, \mathbf{r}_p, \mathbf{v}_p; m_t, \mathbf{r}_t, \mathbf{v}_t} \cdots \int F(\mathbf{r}; m_p, \mathbf{v}_p; m_t, \mathbf{v}_t; m, \mathbf{v}) \\ &\times \delta(\mathbf{r} - \mathbf{r}_p)\delta(\mathbf{r} - \mathbf{r}_t) n(m_p, \mathbf{r}_p, \mathbf{v}_p) n(m_t, \mathbf{r}_t, \mathbf{v}_t) \\ &\times v_{\text{imp}}(\mathbf{r}, \mathbf{v}_p, \mathbf{v}_t)\sigma(m_p, m_t)\, dm_p\, d\mathbf{r}_p\, d\mathbf{v}_p\, dm_t\, d\mathbf{r}_t\, d\mathbf{v}_t.\end{aligned} \tag{3.6}$$

Instead of the function F, we introduce another form of the fragment-generating function $f(m_p, \mathbf{r}_p, \mathbf{v}_p; m_t, \mathbf{r}_t, \mathbf{v}_t; m, \mathbf{r}, \mathbf{v})$ such that $f(\ldots)\, dm\, d\mathbf{r}\, d\mathbf{v}$ is the number of fragments with $[m, m+dm]$, $[\mathbf{r}, \mathbf{r}+d\mathbf{r}]$, $[\mathbf{v}, \mathbf{v}+d\mathbf{v}]$ produced by a collision of particles with $(m_p, \mathbf{r}_p, \mathbf{v}_p)$ and $(m_t, \mathbf{r}_t, \mathbf{v}_t)$. Dimension: $[f(m_p, \mathbf{r}_p, \mathbf{v}_p; m_t, \mathbf{r}_t, \mathbf{v}_t; m, \mathbf{r}, \mathbf{v})] = \text{g}^{-1}\,\text{s}^3\,\text{cm}^{-6}$. Note an essential difference between F and f: the former does not involve radius vectors of the emerging fragments, while the latter does. Notwithstanding normalizing constants, both functions F and f are conditional probabilities. The function F is proportional to the conditional probability of generating a particle with $[m, m+dm]$, $[\mathbf{v}, \mathbf{v}+d\mathbf{v}]$ out of two particles $m_p, \mathbf{v}_p$ and $m_t, \mathbf{v}_t$, provided that both colliders are located at $\mathbf{r}$. Similarly, the function f is proportional to the conditional probability of generating a particle with $[m, m+dm]$, $[\mathbf{r}, \mathbf{r}+d\mathbf{r}]$, $[\mathbf{v}, \mathbf{v}+d\mathbf{v}]$ out of two particles $m_p, \mathbf{r}_p, \mathbf{v}_p$ and $m_t, \mathbf{r}_t, \mathbf{v}_t$, provided that the colliding particles are at the same point in space. This interpretation gives a relation between both functions:

$$\begin{aligned}&f(m_p, \mathbf{r}_p, \mathbf{v}_p; m_t, \mathbf{r}_t, \mathbf{v}_t; m, \mathbf{r}, \mathbf{v})\delta(\mathbf{r}_p - \mathbf{r}_t) \\ &\quad = F(\mathbf{r}; m_p, \mathbf{v}_p; m_t, \mathbf{v}_t; m, \mathbf{v})\delta(\mathbf{r} - \mathbf{r}_p)\delta(\mathbf{r} - \mathbf{r}_t).\end{aligned} \tag{3.7}$$

It is worth noting that the function f is the only quantity in the kinetic equations that determines the collisional outcome (Spahn et al., 2004). Using appropriate definitions of that function, one can easily generalize the equations to include coagulation and restitution. For instance, setting

$$\begin{aligned}&f(m_p, \mathbf{r}_p, \mathbf{v}_p; m_t, \mathbf{r}_t, \mathbf{v}_t; m, \mathbf{r}, \mathbf{v})\delta(\mathbf{r}_p - \mathbf{r}_t) \\ &\quad = \delta\big[m - (m_p + m_t)\big]\delta(\mathbf{r} - \mathbf{r}_p)\delta(\mathbf{r} - \mathbf{r}_t)\delta(\mathbf{v} - \mathbf{v}_c),\end{aligned} \tag{3.8}$$

where $\mathbf{v}_c \equiv (m_p\mathbf{v}_p + m_t\mathbf{v}_t)/(m_p + m_t)$ is the center-of-mass velocity, corresponds to the coagulation case when two colliding particles coalesce. In this paper, however, we restrict ourselves to the fragmentation case.

We now return to Eq. (3.6) and replace the integration over $(\mathbf{r}_p, \mathbf{v}_p; \mathbf{r}_t, \mathbf{v}_t)$ with that over $(\mathbf{p}_p, \mathbf{q}_p; \mathbf{p}_t, \mathbf{q}_t)$. As a result of the transformation of differentials (2.9), the jacobian J appears twice in the equation and, according to (2.11), can be grouped with the n's in the integrand, making these n's functions of the new variables. The impact velocity is a scalar of the transformation; hence we simply replace $v_{\text{imp}}(\mathbf{r}, \mathbf{v}_p, \mathbf{v}_t)$ with $v_{\text{imp}}(\mathbf{p}_p, \mathbf{q}_p; \mathbf{p}_t, \mathbf{q}_t)$, which is the relative speed of two particles with orbital elements given by the arguments, at the collision point. The transformation rule for the function f is the same as for the distribution function n:

$$\begin{aligned}&f(m_p, \mathbf{r}_p, \mathbf{v}_p; m_t, \mathbf{r}_t, \mathbf{v}_t; m, \mathbf{r}, \mathbf{v}) \\ &\quad = f(m_p, \mathbf{p}_p, \mathbf{q}_p; m_t, \mathbf{p}_t, \mathbf{q}_t; m, \mathbf{p}, \mathbf{q})J^{-1},\end{aligned} \tag{3.9}$$

and the jacobian in (3.9) cancels with that in (3.4). We therefore get the following expression for the gain term:

$$\begin{aligned}\left(\frac{dn}{dt}\right)_{\text{gain}}(m, \mathbf{p}, \mathbf{q}) &= \int\limits_{m_p, \mathbf{p}_p, \mathbf{q}_p; m_t, \mathbf{p}_t, \mathbf{q}_t} \cdots \int f(m_p, \mathbf{p}_p, \mathbf{q}_p; m_t, \mathbf{p}_t, \mathbf{q}_t; m, \mathbf{p}, \mathbf{q}) \\ &\times n(m_p, \mathbf{p}_p, \mathbf{q}_p) n(m_t, \mathbf{p}_t, \mathbf{q}_t) v_{\text{imp}}(\mathbf{p}_p, \mathbf{q}_p; \mathbf{p}_t, \mathbf{q}_t) \\ &\times \delta\big[\mathbf{r}(\mathbf{p}_p, \mathbf{q}_p) - \mathbf{r}(\mathbf{p}_t, \mathbf{q}_t)\big]\sigma(m_p, m_t) \\ &\times dm_p\, d\mathbf{p}_p\, d\mathbf{q}_p\, dm_t\, d\mathbf{p}_t\, d\mathbf{q}_t.\end{aligned} \tag{3.10}$$

The transformation of the loss term is done in a similar way, and is even easier because the fragment-generating functions F or f are absent. The final form of the balance equation in terms of the orbital elements is:

$$\frac{dn}{dt}(m, \mathbf{p}, \mathbf{q}) = \left(\frac{dn}{dt}\right)_{\text{gain}}(m, \mathbf{p}, \mathbf{q}) - \left(\frac{dn}{dt}\right)_{\text{loss}}(m, \mathbf{p}, \mathbf{q}) \tag{3.11}$$

with

$$\begin{aligned}\left(\frac{dn}{dt}\right)_{\text{gain}}(m, \mathbf{p}, \mathbf{q}) &= \int\limits_{m_p, \mathbf{p}_p, \mathbf{q}_p; m_t, \mathbf{p}_t, \mathbf{q}_t} \cdots \int f(m_p, \mathbf{p}_p, \mathbf{q}_p; m_t, \mathbf{p}_t, \mathbf{q}_t; m, \mathbf{p}, \mathbf{q}) \\ &\times n(m_p, \mathbf{p}_p, \mathbf{q}_p) n(m_t, \mathbf{p}_t, \mathbf{q}_t) v_{\text{imp}}(\mathbf{p}_p, \mathbf{q}_p; \mathbf{p}_t, \mathbf{q}_t) \\ &\times \delta\big[\mathbf{r}(\mathbf{p}_p, \mathbf{q}_p) - \mathbf{r}(\mathbf{p}_t, \mathbf{q}_t)\big]\sigma(m_p, m_t) \\ &\times dm_p\, d\mathbf{p}_p\, d\mathbf{q}_p\, dm_t\, d\mathbf{p}_t\, d\mathbf{q}_t,\end{aligned} \tag{3.12}$$

$$\begin{aligned}\left(\frac{dn}{dt}\right)_{\text{loss}}(m, \mathbf{p}, \mathbf{q}) &= n(m, \mathbf{p}, \mathbf{q}) \iiint\limits_{m_p, \mathbf{p}_p, \mathbf{q}_p} n(m_p, \mathbf{p}_p, \mathbf{q}_p) \\ &\times v_{\text{imp}}(\mathbf{p}_p, \mathbf{q}_p; \mathbf{p}, \mathbf{q})\delta\big[\mathbf{r}(\mathbf{p}_p, \mathbf{q}_p) - \mathbf{r}(\mathbf{p}, \mathbf{q})\big]\sigma(m_p, m) \\ &\times dm_p\, d\mathbf{p}_p\, d\mathbf{q}_p.\end{aligned} \tag{3.13}$$

Note that the δ-functions in both Eqs. (3.12) and (3.13) represent a collisional condition and are essential. They ensure that the gain and loss terms are being considered in one and the same volume of the "physical" space and thus provide a link between the collisional processes that take place in the "physical" space and distributions in a space of orbital elements. Furthermore, the presence of the δ-functions ($[\delta(\mathbf{r}\cdots)] = \text{cm}^{-3}$) automatically ensures correct dimensionality of the equations: both sides of the equations have dimension $\text{cm}^{-1}\,\text{s}^{-1}\,\text{g}^{-1}$.

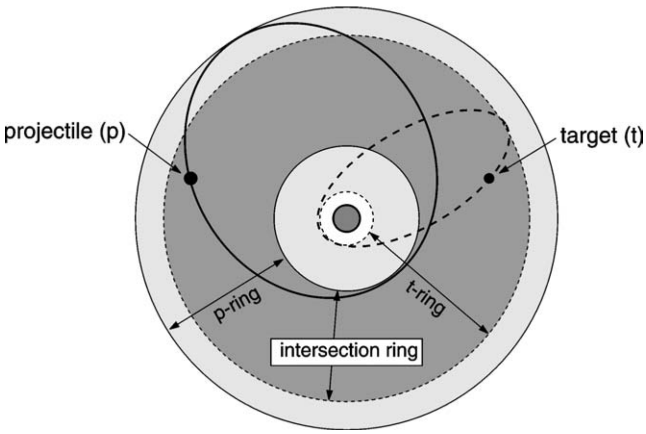

Fig. 3. Representation of colliding particles with rings formed by spreading along the orbits and rotation of lines of nodes and apsides. The rings are shown pole-on.

3.3. Averaging over angular elements

The next step in the derivation is to eliminate from the equations all angles, i.e., variables $\mathbf{q}_p$, $\mathbf{q}_t$, and $\mathbf{q}$. This can be done by integrating all terms in the equations over these variables. Before doing that, it is important to explain the physical meaning of the procedure. An integration over $\mathbf{q}_p$ and $\mathbf{q}_t$ would mean that we "spread" both the projectile particle and the target particle along their orbits and rotate their lines of nodes and apsides over 360° (Fig. 3). Thus we replace each particle with a ring that extends from $a(1-e)$ to $a(1+e)$ radially and from $-\epsilon$ to ϵ latitudinally. For brevity, we will call the rings corresponding to a projectile and a target particle p-ring and t-ring, respectively. The same is true for the collisional debris generated during the impact (not shown in Fig. 3). They can each be thought of as a ring swept by an elliptic orbit with the rotating nodal and apsidal line. This "ring approach" is justified by the fact that in real cosmic disks there are mechanisms that efficiently randomize the orientation of nodes and apsides. The job can be done by the oblateness of the primary (important for planetary rings), by gravity of larger perturbers and, even in non-perturbed disks, by collisions and gravitational encounters. The "ring approach" is similar to that employed by Spaute et al. (1991).

We now integrate both the gain and loss Eqs. (3.12)–(3.13) over $\mathbf{q}$ and substitute (2.7). The left-hand side of either equation just loses the $\mathbf{q}$-argument:

$$\int\limits_{\mathbf{q}} \left(\frac{dn}{dt}\right)(m,\mathbf{p},\mathbf{q})\,d\mathbf{q} = \int\limits_{\mathbf{q}} \varphi(\mathbf{q})\left(\frac{dn}{dt}\right)(m,\mathbf{p})\,d\mathbf{q} = \left(\frac{dn}{dt}\right)(m,\mathbf{p}). \tag{3.14}$$

Before transforming the right-hand sides, we introduce the following averages:

$$\begin{aligned}\overline{v_{\mathrm{imp}}}(\mathbf{p}_p,\mathbf{p}_t) &\equiv \langle v_{\mathrm{imp}}\rangle_{\mathbf{q}_p,\mathbf{q}_t}\\ &\equiv \left(\iint\limits_{\mathbf{q}_p\mathbf{q}_t} v_{\mathrm{imp}}(\mathbf{p}_p,\mathbf{q}_p,\mathbf{p}_t,\mathbf{q}_t)\delta\big[\mathbf{r}(\mathbf{p}_p,\mathbf{q}_p)-\mathbf{r}(\mathbf{p}_t,\mathbf{q}_t)\big]\right.\\ &\quad\left.\times\,\varphi(\mathbf{q}_p)\varphi(\mathbf{q}_t)\,d\mathbf{q}_p\,d\mathbf{q}_t\right)\\ &\quad\times\left(\iint\limits_{\mathbf{q}_p\mathbf{q}_t}\delta\big[\mathbf{r}(\mathbf{p}_p,\mathbf{q}_p)-\mathbf{r}(\mathbf{p}_t,\mathbf{q}_t)\big]\varphi(\mathbf{q}_p)\right.\\ &\quad\left.\times\,\varphi(\mathbf{q}_t)\,d\mathbf{q}_p\,d\mathbf{q}_t\right)^{-1}\end{aligned} \tag{3.15}$$

and

$$\begin{aligned}&\bar f(m_p,\mathbf{p}_p;m_t,\mathbf{p}_t;m,\mathbf{p})\\ &\quad\equiv\int\limits_{\mathbf{q}}\langle f\rangle_{\mathbf{q}_p,\mathbf{q}_t}\,d\mathbf{q}\\ &\quad\equiv\int\limits_{\mathbf{q}}\left(\iint\limits_{\mathbf{q}_p\mathbf{q}_t} f(m_p,\mathbf{p}_p;\mathbf{q}_p m_t,\mathbf{p}_t,\mathbf{q}_t;m,\mathbf{p},\mathbf{q})\right.\\ &\qquad\left.\times\,\delta\big[\mathbf{r}(\mathbf{p}_p,\mathbf{q}_p)-\mathbf{r}(\mathbf{p}_t,\mathbf{q}_t)\big]\varphi(\mathbf{q}_p)\varphi(\mathbf{q}_t)\,d\mathbf{q}_p\,d\mathbf{q}_t\right)\\ &\qquad\times\left(\iint\limits_{\mathbf{q}_p\mathbf{q}_t}\delta\big[\mathbf{r}(\mathbf{p}_p,\mathbf{q}_p)-\mathbf{r}(\mathbf{p}_t,\mathbf{q}_t)\big]\varphi(\mathbf{q}_p)\right.\\ &\qquad\left.\times\,\varphi(\mathbf{q}_t)\,d\mathbf{q}_p\,d\mathbf{q}_t\right)^{-1}d\mathbf{q}.\end{aligned} \tag{3.16}$$

The meaning of $\overline{v_{\mathrm{imp}}}$ is obvious, and $\bar f(m_p,\mathbf{p}_p;m_t,\mathbf{p}_t;m,\mathbf{p})\,dm\,d\mathbf{p}$ is the number of fragments with $[m,m+dm]$, $[\mathbf{p},\mathbf{p}+d\mathbf{p}]$, produced by a collision of particles with $(m_p,\mathbf{p}_p)$ and $(m_t,\mathbf{p}_t)$.

The integral that appears in the denominators,

$$\Delta(\mathbf{p}_p,\mathbf{p}_t)\equiv\iint\limits_{\mathbf{q}_p\mathbf{q}_t}\delta\big[\mathbf{r}(\mathbf{p}_p,\mathbf{q}_p)-\mathbf{r}(\mathbf{p}_t,\mathbf{q}_t)\big] \times\varphi(\mathbf{q}_p)\varphi(\mathbf{q}_t)\,d\mathbf{q}_p\,d\mathbf{q}_t, \tag{3.17}$$

has the following geometrical interpretation: it is *approximately* the volume of the intersection between the p-ring and the t-ring divided by the volumes of both rings. (Approximately—because a strict calculation of the integral will take into account that the motion of particles in elliptic orbits is not uniform and therefore, automatically "weight" the volumes.) Accordingly, the dimension is $[\Delta]=\mathrm{cm}^{-3}$.

The transformation of the right-hand side of the gain term gives:

$$\begin{aligned}&\left(\frac{dn}{dt}\right)_{\mathrm{gain}}(m,\mathbf{p})\\ &\quad=\int\limits_{\mathbf{q}}d\mathbf{q}\int\limits_{\substack{m_p,\mathbf{p}_p,\mathbf{q}_p;\\ m_t,\mathbf{p}_t,\mathbf{q}_t}}\cdots\int f(m_p,\mathbf{p}_p,\mathbf{q}_p;m_t,\mathbf{p}_t,\mathbf{q}_t;m,\mathbf{p},\mathbf{q})\\ &\qquad\times n(m_p,\mathbf{p}_p)\varphi(\mathbf{q}_p)n(m_t,\mathbf{p}_t)\varphi(\mathbf{q}_t)v_{\mathrm{imp}}(\mathbf{p}_p,\mathbf{q}_p;\mathbf{p}_t,\mathbf{q}_t)\\ &\qquad\times\delta\big[\mathbf{r}(\mathbf{p}_p,\mathbf{q}_p)-\mathbf{r}(\mathbf{p}_t,\mathbf{q}_t)\big]\sigma(m_p,m_t)\end{aligned}$$

$$\times\, dm_p\, d\mathbf{p}_p\, d\mathbf{q}_p\, dm_t\, d\mathbf{p}_t\, d\mathbf{q}_t. \tag{3.18}$$

We now *make a simplification*: replace the impact velocity v_{imp} with $\overline{v_{\text{imp}}}$ given by (3.15), resulting in

$$\left(\frac{dn}{dt}\right)_{\text{gain}}(m,\mathbf{p}) \approx \int_{\mathbf{q}} d\mathbf{q} \int\cdots\int_{\substack{m_p,\mathbf{p}_p,\mathbf{q}_p;\\ m_t,\mathbf{p}_t,\mathbf{q}_t}} f(m_p,\mathbf{p}_p,\mathbf{q}_p;m_t,\mathbf{p}_t,\mathbf{q}_t;m,\mathbf{p},\mathbf{q}) \times \delta\big[\mathbf{r}(\mathbf{p}_p,\mathbf{q}_p)-\mathbf{r}(\mathbf{p}_t,\mathbf{q}_t)\big]\varphi(\mathbf{q}_p)\varphi(\mathbf{q}_t)n(m_p,\mathbf{p}_p) \times n(m_t,\mathbf{p}_t)\overline{v_{\text{imp}}}(\mathbf{p}_p,\mathbf{p}_t)\sigma(m_p,m_t) \times dm_p\, d\mathbf{p}_p\, d\mathbf{q}_p\, dm_t\, d\mathbf{p}_t\, d\mathbf{q}_t \tag{3.19}$$

or, using (3.16),

$$\left(\frac{dn}{dt}\right)_{\text{gain}}(m,\mathbf{p}) = \iiiint_{m_p,m_t,\mathbf{p}_p,\mathbf{p}_t} \bar{f}(m_p,\mathbf{p}_p;m_t,\mathbf{p}_t;m,\mathbf{p}) \times n(m_p,\mathbf{p}_p)n(m_t,\mathbf{p}_t)\overline{v_{\text{imp}}}(\mathbf{p}_p,\mathbf{p}_t) \times \Delta(\mathbf{p}_p,\mathbf{p}_t)\sigma(m_p,m_t) \times dm_p\, dm_t\, d\mathbf{p}_p\, d\mathbf{p}_t. \tag{3.20}$$

The right-hand side of the loss term transforms without any simplifications:

$$\left(\frac{dn}{dt}\right)_{\text{loss}}(m,\mathbf{p}) = \int_{\mathbf{q}} d\mathbf{q}\, n(m,\mathbf{p})\varphi(\mathbf{q}) \iiint_{m_p,\mathbf{p}_p,\mathbf{q}_p} n(m_p,\mathbf{p}_p)\varphi(\mathbf{q}_p) \times v_{\text{imp}}(\mathbf{p}_p,\mathbf{q}_p;\mathbf{p},\mathbf{q})\delta\big[\mathbf{r}(\mathbf{p}_p,\mathbf{q}_p)-\mathbf{r}(\mathbf{p},\mathbf{q})\big]\sigma(m_p,m) \times dm_p\, d\mathbf{p}_p\, d\mathbf{q}_p \tag{3.21}$$

or, using (3.15),

$$\left(\frac{dn}{dt}\right)_{\text{loss}}(m,\mathbf{p}) = n(m,\mathbf{p}) \iint_{m_p,\mathbf{p}_p} n(m_p,\mathbf{p}_p)\overline{v_{\text{imp}}}(\mathbf{p}_p,\mathbf{p})\Delta(\mathbf{p}_p,\mathbf{p}) \times \sigma(m_p,m)\, dm_p\, d\mathbf{p}_p. \tag{3.22}$$

Collecting together Eqs. (3.11), (3.14), (3.20), and (3.22), the equations take the final form:

$$\frac{dn}{dt}(m,\mathbf{p}) = \left(\frac{dn}{dt}\right)_{\text{gain}}(m,\mathbf{p}) - \left(\frac{dn}{dt}\right)_{\text{loss}}(m,\mathbf{p}), \tag{3.23}$$

$$\left(\frac{dn}{dt}\right)_{\text{gain}}(m,\mathbf{p}) = \iiiint_{m_p,m_t,\mathbf{p}_p,\mathbf{p}_t} \bar{f}(m_p,\mathbf{p}_p;m_t,\mathbf{p}_t;m,\mathbf{p}) \times n(m_p,\mathbf{p}_p)n(m_t,\mathbf{p}_t)\overline{v_{\text{imp}}}(\mathbf{p}_p,\mathbf{p}_t) \times \Delta(\mathbf{p}_p,\mathbf{p}_t)\sigma(m_p,m_t) \times dm_p\, dm_t\, d\mathbf{p}_p\, d\mathbf{p}_t, \tag{3.24}$$

$$\left(\frac{dn}{dt}\right)_{\text{loss}}(m,\mathbf{p}) = n(m,\mathbf{p}) \iint_{m_p,\mathbf{p}_p} n(m_p,\mathbf{p}_p)\overline{v_{\text{imp}}}(\mathbf{p}_p,\mathbf{p}) \times \Delta(\mathbf{p}_p,\mathbf{p})\sigma(m_p,m)\, dm_p\, d\mathbf{p}_p. \tag{3.25}$$

The reciprocal of the integral in Eq. (3.25) is the collisional lifetime of particles with mass m and orbital elements $\mathbf{p}$, which we denote $T(m,\mathbf{p})$. One can introduce an average collisional lifetime of particles of mass m by

$$T(m) \equiv \left[\frac{\int_{\mathbf{p}} T^{-1}(m,\mathbf{p})n(m,\mathbf{p})\, d\mathbf{p}}{\int_{\mathbf{p}} n(m,\mathbf{p})\, d\mathbf{p}}\right]^{-1}. \tag{3.26}$$

3.4. *Additional averaging over inclination*

Equations (3.23)–(3.25) determine the 4-argument phase space distribution function $n(m,\mathbf{p}) \equiv n(m,a,e,i)$. For the sake of speeding up the calculations, and taking into account that in many applications the evolution of i is of less importance than that of a and e, we will further reduce the dimension of the phase space by performing averaging over the inclination. Such a "thin-disk" approximation involves a phase space distribution with 3 arguments, $n(m,a,e)$. Luckily, no additional derivation is required to obtain equations for $n(m,a,e)$—it is sufficient to redefine vectors $\mathbf{p}$ and $\mathbf{q}$ in the equations already obtained. We now put $\mathbf{p} \equiv (a,e)$ and $\mathbf{q} \equiv (i,\Omega,\omega,M)$. Then the whole derivation given in the previous subsection can be repeated without any changes for this set of elements, yielding the same Eqs. (3.23)–(3.25).

Throughout the rest of the paper, we will assume that $\mathbf{p} = (a,e)$. However, it is important to know that Eqs. (3.23)–(3.25) have a covariant form. Instead of Keplerian elements, one can use any other set of 6 quantities that fully determine the particle's state—for instance, Delaunay or Poincaré variables. "Splitting" of those six between $\mathbf{p}$ and $\mathbf{q}$ is also arbitrary. For example, setting $\mathbf{p} \equiv a$ and averaging over $\mathbf{q} \equiv (e,i,\Omega,\omega,M)$ would result in a model focused on the mass-distance distribution of material. Regardless of the choice of $\mathbf{p}$ and $\mathbf{q}$, the system is described by Eqs. (3.23)–(3.25).

3.5. *Corrections for the gravitational interaction of particles*

For larger objects, it may be necessary to take into account their mutual gravitational interaction before collision. Gravity enhances the collisional cross section (Safronov's factor) and increases the impact velocity. Then, the product $\sigma(m_p,m_t)\overline{v_{\text{imp}}}(\mathbf{p}_p,\mathbf{p}_t)$ in Eqs. (3.24) and (3.25) should be replaced with

$$\sigma(m_p,m_t)\overline{v_{\text{imp}}}(\mathbf{p}_p,\mathbf{p}_t)\left(1+\frac{v_{\text{esc}}^2}{v_{\text{imp}}^2}\right)^{3/2}, \tag{3.27}$$

where

$$v_{\text{esc}} = \sqrt{\frac{2G(m_p+m_t)}{s_p+s_t}}. \tag{3.28}$$

The mutual gravity will also affect integration domains in the equations discussed below, because an increase in the impact velocity changes the minimum mass of the shattering projectile, m_{cr}, and the mass of the largest collisional fragment, m_x, discussed in Section 5.

3.6. Argument ranges and integration domains

The range of $(m, \mathbf{p}) \equiv (m, a, e)$ in Eqs. (3.23)–(3.25) is:

$$0 \leqslant m \leqslant \infty, \qquad 0 \leqslant a \leqslant \infty, \qquad 0 \leqslant e < 1. \tag{3.29}$$

The integration domain in the gain term (3.24) is:

$$0 \leqslant m_p \leqslant m_t \leqslant \infty, \qquad 0 \leqslant a_p, a_t \leqslant \infty,$$
$$0 \leqslant e_p, e_t < 1 \tag{3.30}$$

(note the condition $m_p \leqslant m_t$), to which two additional requirements are added: the particles should be in collisional orbits and the projectile should carry enough energy to disrupt the target. The first condition means an overlap between the p- and t-rings and reduces to

$$a_p(1 - e_p) < a_t(1 + e_t) \quad \text{and} \quad a_p(1 + e_p) > a_t(1 - e_t), \tag{3.31}$$

while the second can be written as

$$m_{cr} \leqslant m_p, \tag{3.32}$$

where $m_{cr}(m_p, m_t, \overline{v_{\mathrm{imp}}}(\mathbf{p}_p, \mathbf{p}_t))$ is the minimum mass of a projectile that destroys the grain of mass m_t.

Similarly, the integration domain in the loss term (3.25) is:

$$0 \leqslant m_p \leqslant \infty, \qquad 0 \leqslant a_p \leqslant \infty, \qquad 0 \leqslant e_p < 1 \tag{3.33}$$

with additional conditions

$$a_p(1 - e_p) < a(1 + e), \qquad a_p(1 + e_p) > a(1 - e) \tag{3.34}$$

and

$$m_{cr} \leqslant m_p, \tag{3.35}$$

where $m_{cr} = m_{cr}(m_p, m, \overline{v_{\mathrm{imp}}}(\mathbf{p}_p, \mathbf{p}))$.

4. Probability and kinematics of a binary collision

Equations (3.24) and (3.25) contain two functions, $\Delta(\mathbf{p}_p, \mathbf{p}_t)$ and $\overline{v_{\mathrm{imp}}}(\mathbf{p}_p, \mathbf{p}_t)$, which depend solely on the p- and t-rings representing two colliding particles. The first function, Δ, basically determines the probability of collision for a pair of crossing Keplerian orbits (cf. K_R in Eq. (5) of Spaute et al., 1991). The second function, $\overline{v_{\mathrm{imp}}}$, tells us how strong the collision will be. Neither of them "cares" about the outcome of that collision, however. This is why both quantities are independent of the masses of the colliders.

A complication of calculating the quantities in question stems from the fact that here, unlike in other parts of the model, we cannot ignore the third spatial dimension related to particles' orbital inclinations and nodes. There is no simple scaling for probabilities of collisions and relative velocities for disks with different semi-opening angles ϵ.

4.1. The integral Δ

We now consider the integral (3.17):

$$\Delta(\mathbf{p}_p, \mathbf{p}_t) \equiv \iint\limits_{\mathbf{q}_p \mathbf{q}_t} \delta\big[\mathbf{r}(\mathbf{p}_p, \mathbf{q}_p) - \mathbf{r}(\mathbf{p}_t, \mathbf{q}_t)\big] \times \varphi(\mathbf{q}_p)\varphi(\mathbf{q}_t)\, d\mathbf{q}_p\, d\mathbf{q}_t. \tag{4.1}$$

In the 2D case (disk semi-opening angle $\epsilon = 0$), the Δ-integral can be reduced to a single integral over a function of the true anomaly of one of the two particles. Including the third dimension ($\epsilon > 0$) further complicates the integral. In any event, the resulting integral is not elementary and must be calculated numerically, which would slow down the calculations drastically. Thus we have to use an approximation.

As noted above, the integral is approximately the volume of the intersection between the p-ring and the t-ring, A_{pt}, divided by the volumes of both rings, A_p and A_t:

$$\Delta(\mathbf{p}_p, \mathbf{p}_t) \approx \frac{A_{pt}}{A_p A_t}. \tag{4.2}$$

Denote by $A(r_{\min}, r_{\max})$ the volume of the disk between the distances $r_{\min}$ and $r_{\max}$ ($r_{\min} < r_{\max}$):

$$A(r_{\min}, r_{\max}) = \frac{4}{3}\pi\left(r_{\max}^3 - r_{\min}^3\right)\sin\varepsilon. \tag{4.3}$$

Obviously,

$$A_p = A\big(a_p(1 - e_p), a_p(1 + e_p)\big),$$
$$A_t = A\big(a_t(1 - e_t), a_t(1 + e_t)\big) \tag{4.4}$$

and it only remains to find A_{pt}.

All possible cases are sketched in Fig. 4. If the rings overlap, Eq. (3.31), we set

$$r_{\min} = \max\big[a_p(1 - e_p), a_t(1 - e_t)\big],$$

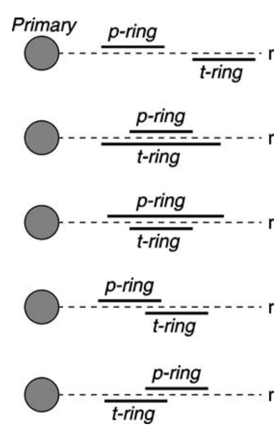

Fig. 4. Location of p- and t-rings.

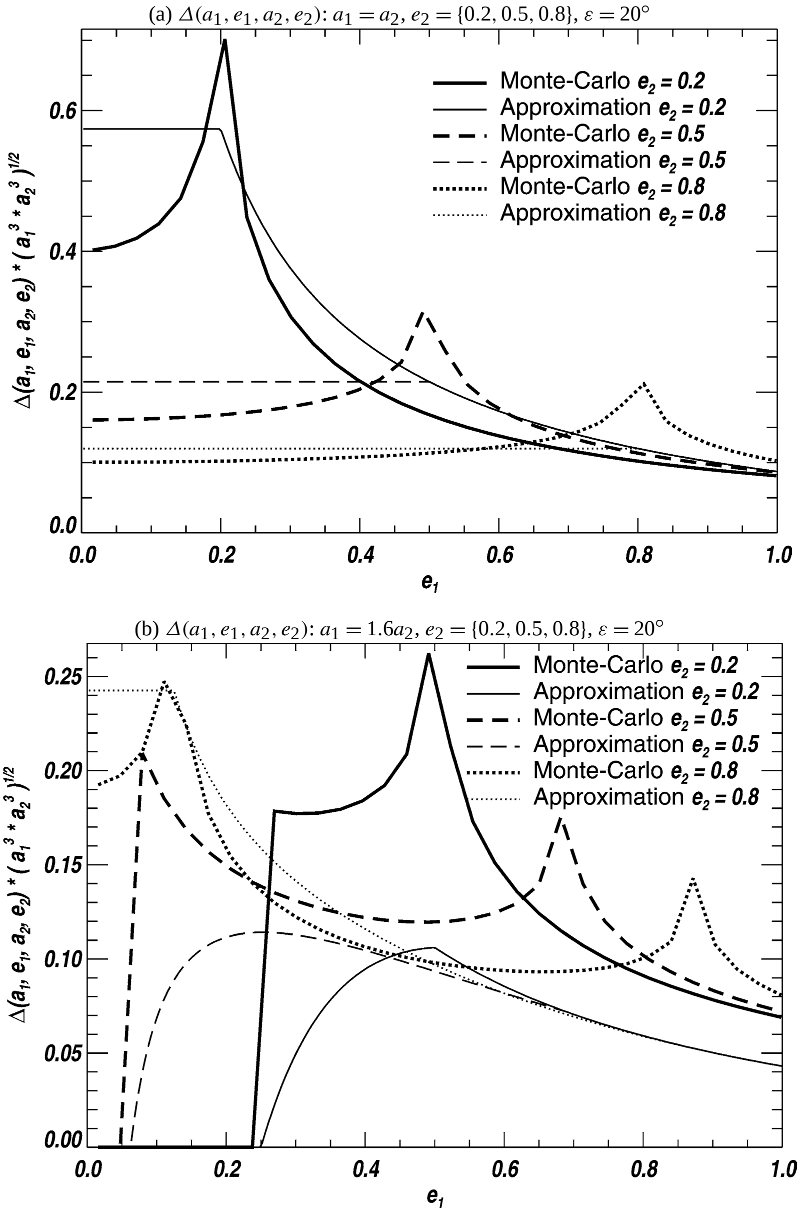

Fig. 5. The Δ integral for different combinations of the semimajor axes and eccentricities of two colliding particles, a_1, e_1, a_2, e_2. (Top) $a_1 = a_2$, (bottom) $a_1 = 1.6a_2$ (see legend for other parameters). We show the results for one value of the disk's semi-opening angle $\epsilon = 20°$. The results for other values look similar. For each set of a_1, e_1, a_2, e_2, two values are shown: "exact" (obtained with time-consuming Monte Carlo evaluation of the Δ-integral, a thick line) and approximate (our geometrical approximation, Eq. (4.2), a thin line of the same style).

$$r_{\max} = \min\left[a_p(1+e_p), a_t(1+e_t)\right] \tag{4.5}$$

and

$$A_{pt} = A(r_{\min}, r_{\max}), \tag{4.6}$$

where the function A is given by Eq. (4.3). For non-overlapping rings, we have simply $A_{pt} = 0$ and $\Delta = 0$.

Using an "exact" Monte Carlo evaluation of the integral (4.1), we checked the accuracy of the geometrical approximation presented here. Typical results of this comparison are shown in Fig. 5. The geometrical approximation typically provides a 10–30% accuracy and only in some pathological cases underestimates the true value by a factor of two.

4.2. Impact velocity v_{imp}

Consider two "rings" (a_p, e_p) and (a_t, e_t) crossing each other, i.e., satisfying Eq. (3.31). We are interested in the averaged impact velocity $\overline{v_{\mathrm{imp}}}(\mathbf{p}_p, \mathbf{p}_t)$, given by Eq. (3.15):

$$\overline{v_{\mathrm{imp}}}(\mathbf{p}_p, \mathbf{p}_t) = \frac{1}{\Delta(\mathbf{p}_p, \mathbf{p}_t)} \iint\limits_{\mathbf{q}_p \mathbf{q}_t} v_{\mathrm{imp}}(\mathbf{p}_p, \mathbf{q}_p, \mathbf{p}_t, \mathbf{q}_t) \times \delta\left[\mathbf{r}(\mathbf{p}_p, \mathbf{q}_p) - \mathbf{r}(\mathbf{p}_t, \mathbf{q}_t)\right] \times \varphi(\mathbf{q}_p)\varphi(\mathbf{q}_t)\, d\mathbf{q}_p\, d\mathbf{q}_t. \tag{4.7}$$

According to this definition, a strict way to compute it would be to calculate the integral Δ twice—with and without v_{imp}

in the integrand—and taking the ratio. As noted above, a direct evaluation of the Δ-integrals would be too cumbersome computationally, so we use approximate solutions again.

The simplest approximation is a "particle-in-a-box" formula

$$\overline{v_{\rm imp}}^2(a_p, e_p, a_t, e_t) = \frac{2G\mathcal{M}}{a_p + a_t}\left(e_p^2 + e_t^2 + \sin^2\epsilon\right), \tag{4.8}$$

where $\mathcal{M}$ is the mass of the central body and ϵ is the semi-opening angle of the disk, so that the last term in parentheses reflects the relative velocity coming from the orbital inclinations of the particles.

A better approximation can be obtained in the following way. Kholshevnikov and Shor (1994) solved a similar problem in a 3D case, employing, however, an averaging procedure which is not symmetric with respect to both colliding particles. In the spirit of their approach, one can obtain (M. Sremčević, in preparation)

$$\begin{aligned}\overline{v_{\rm imp}}(\mathbf{p}_p, \mathbf{p}_t) = 1/2\big(&v_{\rm KS}(a_p, e_p, a_t, e_t)\\ &+ v_{\rm KS}(a_t, e_t, a_p, e_p)\big),\end{aligned} \tag{4.9}$$

where

$$\begin{aligned}&v_{\rm KS}^2(a_1, e_1, a_2, e_2)\\ &\quad= \frac{G\mathcal{M}}{p_1}\Bigg[3 - \frac{p_1}{a_2} + e_1^2 - \left(2 + e_1^2\right)\overline{\cos i}\sqrt{\frac{p_2}{p_1}}\\ &\qquad + 4e_1\frac{\sin l_2 - \sin l_1}{l_2 - l_1}\left(1.0 - \overline{\cos i}\sqrt{\frac{p_2}{p_1}}\right)\\ &\qquad - \frac{1}{2}e_1^2\frac{\sin(2l_2) - \sin(2l_1)}{l_2 - l_1}\overline{\cos i}\sqrt{\frac{p_2}{p_1}}\Bigg].\end{aligned} \tag{4.10}$$

Here, $p_1 = a_1(1 - e_1^2)$ and $p_2 = a_2(1 - e_2^2)$ are the *semilatera recta* of the two orbits, and

$$\overline{\cos i} = \int_0^\epsilon \cos i\,\phi(i)\,di \tag{4.11}$$

is the mean inclination, which for a uniform distribution of inclinations (2.20) is simply

$$\overline{\cos i} = \frac{\sin^2\epsilon}{2(1 - \cos\epsilon)}. \tag{4.12}$$

The quantities l_1 and l_2 are given by

$$\begin{aligned} l_1 &= \begin{cases} 0 & \text{if } a_1(1 - e_1) \geqslant a_2(1 - e_2),\\ \arccos\left[\frac{1}{e_1}\left(\frac{p_1}{a_2(1 - e_2)} - 1\right)\right] & \text{otherwise,}\end{cases}\\ l_2 &= \begin{cases} \pi & \text{if } a_1(1 + e_1) \leqslant a_2(1 + e_2),\\ \arccos\left[\frac{1}{e_1}\left(\frac{p_1}{a_2(1 + e_2)} - 1\right)\right] & \text{otherwise.}\end{cases}\end{aligned} \tag{4.13}$$

Remember that we require that the two rings overlap, Eq. (3.31).

As in the case of the Δ-integral, we used direct Monte Carlo evaluation of the integral (4.7) to check the accuracy of both Eq. (4.8) and Eq. (4.9). Typical results of this comparison are shown in Fig. 6. The particle-in-a-box formula (4.8) still provides reasonable accuracy for moderate eccentricities, but severely underestimates the impact velocity for high e. Our alternative, Eq. (4.9), does an excellent job, providing better than 10% accuracy in nearly all the cases.

5. Impact mechanics

As explained above, the quantities analyzed in the previous section do not "care" about the outcome of a binary collision. Now we focus on terms that describe the mechanics of such a collision, assuming it to be destructive. These are the minimum mass of the shattering impactor, the mass of the largest collisional fragment, as well as the distribution of masses and orbital elements of the collisional fragments. These quantities appear both in integrands and integration domains of Eqs. (3.24) and (3.25). They rely on the so-called critical energy for fragmentation, discussed immediately below.

5.1. *The critical specific energy*

As a conventional "threshold" between the cratering collisions (which we do not consider here) and disruptive ones (which are of central interest for this work), one usually considers the case where the mass of the largest particle left after the impact is half the target mass: $m_x = 0.5m_t$ (see, e.g., Paolicchi et al., 1996; Durda et al., 1998; Benz and Asphaug, 1999). The kinetic energy of the projectile per unit target's mass, required for such a "marginally disruptive" impact, is called the *critical specific energy* and denoted Q_D^*. By definition, this quantity includes the energy needed for both disruption of the target (work against strength) and dispersal of the collisional fragments to the "local infinity" (work against gravity)—see Durda et al. (1998). Later we shall see that knowledge of Q_D^* is required to calculate both m_{cr} and m_x.

The critical specific energy is known to be a function of the target radius s_t (or its mass m_t), essentially consisting of two power laws (see, e.g., Davis et al., 1985; Holsapple, 1994; Paolicchi et al., 1996; Durda and Dermott, 1997; Durda et al., 1998; Benz and Asphaug, 1999; Kenyon and Bromley, 2004b):

$$Q_D^*(s_t) = A_s s_t^{b_s} + A_g s_t^{b_g}. \tag{5.1}$$

The first one, with a shallow negative slope, dominates in the strength regime at smaller sizes. The second one controls the fragmentation of larger objects and has a positive index between 1 and 2, reflecting the growth of gravitational binding energy of large objects with their size. Absolute values of constants in Eq. (5.1) can be found in the papers cited above. For a visual comparison of differ-

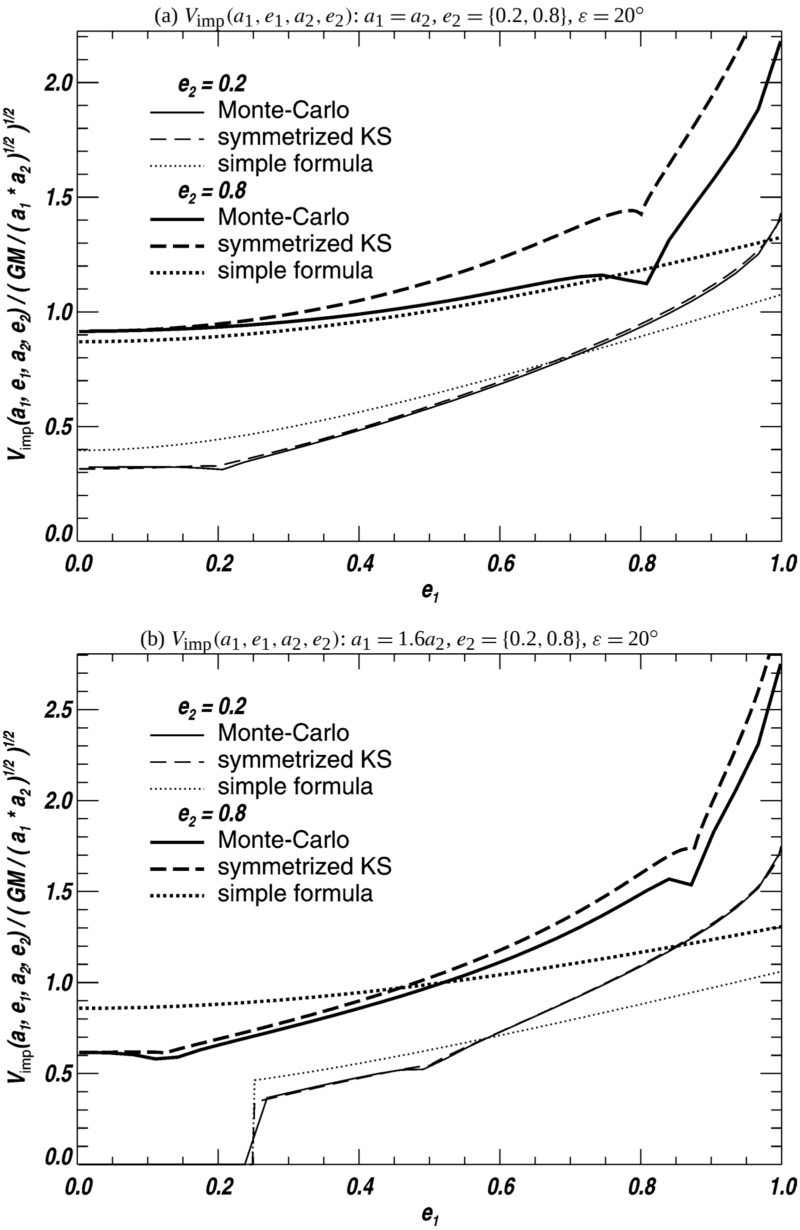

Fig. 6. The average impact velocity $\overline{v_{\rm imp}}$ for different combinations of the semimajor axes and eccentricities of two colliding particles, a_1, e_1, a_2, e_2. The figure is organized similarly to Fig. 5, expect that we compare three and not two different computation methods here. For each set of a_1, e_1, a_2, e_2, we show: "exact" results (obtained with time-consuming Monte Carlo evaluation of the Δ-integral, solid lines), results from Eqs. (4.9)–(4.10) (dashed lines), and those from Eq. (4.8) (dotted lines).

ent curves see, e.g., Figs. 1 and 5 in Durda et al. (1998), Fig. 8 in Benz and Asphaug (1999), and Fig. 1 in Kenyon and Bromley (2004b). Most of the studies report a minimum of Q_D^* to lie at radius ~ 0.1 km. However, for a given size, material, and impact speed, the absolute values reported differ by at least one order of magnitude. Besides, actual values for astronomical objects, such as EKBOs, may deviate from those found in laboratory or by hydrocode simulations, due to the objects' complex internal structure and porosity. From the available literature, we have chosen two model materials, a weaker one ("ice") and a stronger one ("rock"), for which Q_D^* and constants are depicted in Fig. 7.

5.2. The minimum projectile mass m_{cr}

Consider a collision of two grains: $(m_p, \mathbf{p}_p)$ and $(m_t, \mathbf{p}_t)$. From the definition of the critical specific energy, the minimum mass of a projectile that destroys the target satisfies the equation

$$\frac{m_t m_{cr}}{m_t + m_{cr}} \frac{\overline{v_{\rm imp}}^2}{2} = m_t Q_D^*(m_t) + m_{cr} Q_D^*(m_{cr}). \tag{5.2}$$

Here, the left-hand side is the available impact energy (see Eq. (5.13) below), assumed to be entirely spent for disruption and dispersal, and the right-hand side is the energy needed to disrupt and disperse both colliders. Taking into

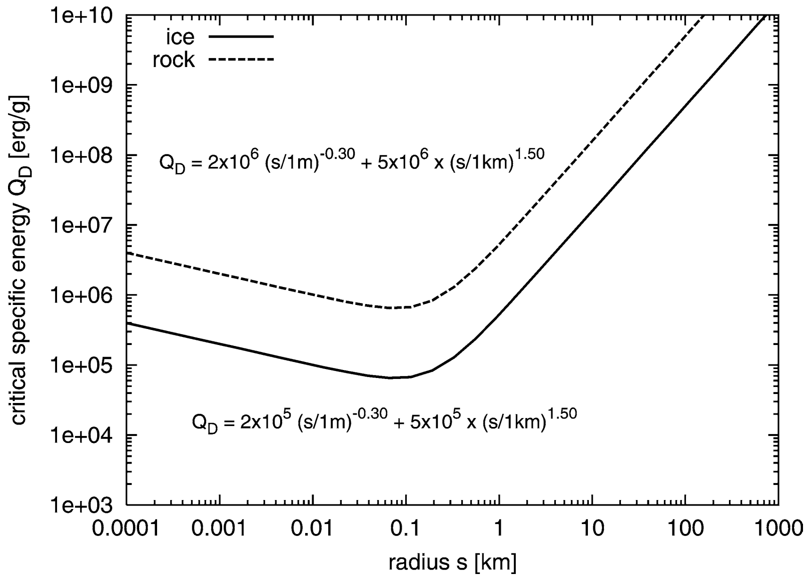

Fig. 7. Dependence of the critical specific energy for fragmentation on the target particle's radius. Solid curve: weaker material ("ice"), dashed: stronger material ("rock").

account that usually $m_{cr} \ll m_t$, Eq. (5.2) can be replaced by

$$\frac{m_{cr}\overline{v_{\mathrm{imp}}}^2}{2} \approx m_t Q_D^*(m_t). \tag{5.3}$$

For objects in the strength regime and impact velocities of order $1\,\mathrm{km\,s^{-1}}$, the minimum projectile mass (size) is 3 (1) order(s) of magnitude less than that of the target. Obviously, $m_{cr} = m_{cr}(m_t, \overline{v_{\mathrm{imp}}}(\mathbf{p}_p, \mathbf{p}_t)) = m_{cr}(\mathbf{p}_p; m_t, \mathbf{p}_t)$.

5.3. *The mass of the largest fragment m_x*

Consider again a collision of two grains: $(m_p, \mathbf{p}_p)$ and $(m_t, \mathbf{p}_t)$. In what follows, we will need to know the largest fragment's mass m_x. An approximate scaling law for m_x is (e.g., Paolicchi et al., 1996) $m_x/m_t \propto E_p^{-c}$, where E_p is the kinetic energy of the projectile and c is a constant close to unity. In extended form,

$$\frac{m_x}{m_t} = \frac{1}{2}\left[2\frac{m_t}{m_p}\frac{Q_D^*(m_t)}{\overline{v_{\mathrm{imp}}}^2}\right]^c, \tag{5.4}$$

where the normalization is consistent with Eq. (5.3). Of course, Eq. (5.4) implies $m_p \geqslant m_{cr}(m_t)$, resulting in $m_x \leqslant (1/2)m_t$. For the two materials used in our modeling, we assume $c = 0.91$ for "ice" (Arakawa, 1999) and $c = 1.24$ for "rock" (Paolicchi et al., 1996). The larger the impact energy, the smaller the fragments. For two objects of the same size (in the strength regime), for impact velocities of the order of $1\,\mathrm{km\,s^{-1}}$, the largest fragment's mass is a factor of thousand smaller than the original mass of either collider. The functional dependence of m_x is: $m_x = m_x(m_p, m_t, \overline{v_{\mathrm{imp}}}(\mathbf{p}_p, \mathbf{p}_t)) = m_x(m_p, \mathbf{p}_p; m_t, \mathbf{p}_t)$.

5.4. *Production of collisional fragments: the function $\bar{f}$*

Consider the function $\bar{f}$ that appears in the gain term (3.24). As noted above, $\bar{f}(m_p, \mathbf{p}_p; m_t, \mathbf{p}_t; m, \mathbf{p})\,dm\,d\mathbf{p}$ is the number of fragments with $[m, m+dm]$, $[\mathbf{p}, \mathbf{p}+d\mathbf{p}]$, produced in a collision of particles with $(m_p, \mathbf{p}_p)$ and $(m_t, \mathbf{p}_t)$.

The function $\bar{f}$ includes two distributions: the mass distribution of fragments and the distribution of their orbital elements. Omitting for brevity the quantities with indices p and t, we can write:

$$\bar{f}(m, \mathbf{p}) \equiv \bar{g}(m)\bar{h}(m, \mathbf{p}) \tag{5.5}$$

and split $\bar{f}$ into that product in such a way that $\bar{g}(m)\,dm$ is the number of fragments with masses $[m, m+dm]$, whereas $\bar{h}(m, \mathbf{p})\,d\mathbf{p}$ is the fraction (by number) of fragments with mass m that have elements $[\mathbf{p}, \mathbf{p}+d\mathbf{p}]$. The normalizations of $\bar{g}$ and $\bar{h}$ are

$$\int_0^{m_x} m\bar{g}(m)\,dm = m_p + m_t \tag{5.6}$$

and

$$\int_{\mathbf{p}} \bar{h}(m, \mathbf{p})\,d\mathbf{p} = 1, \tag{5.7}$$

whence the normalization of $\bar{f}$ is

$$\int_0^{m_x}\int_{\mathbf{p}} m\bar{f}(m, \mathbf{p})\,dm\,d\mathbf{p} = \int_0^{m_x} m\bar{g}(m)\left[\int_{\mathbf{p}} \bar{h}(m, \mathbf{p})\,d\mathbf{p}\right]dm = m_p + m_t. \tag{5.8}$$

5.5. *Mass distribution of collisional fragments: the function $\bar{g}$*

For the mass distribution function, we adopt

$$\bar{g}(m_p, \mathbf{p}_p; m_t, \mathbf{p}_t; m) = G(m_p, \mathbf{p}_p; m_t, \mathbf{p}_t) m^{-\eta}, \quad 0 < m \leqslant m_x \tag{5.9}$$

with

$$G(m_p, \mathbf{p}_p; m_t, \mathbf{p}_t) = (2-\eta)(m_p + m_t) m_x^{\eta-2} \quad (\eta < 2). \tag{5.10}$$

Plausible values of η from impact experiments are 1.5, ..., 2.0; a "classical" value is $11/6 = 1.83$ (corresponds to a differential size distribution with the index 3.5). Equation (5.10) ensures correct normalization: Eq. (5.6) is satisfied. The function G depends on the $\mathbf{p}$'s because m_x does.

5.6. *Orbital distribution of collisional fragments: the function $\bar{h}$*

To write the function $\bar{h}$, we need to know the orbital elements of collisional fragments. We start with a few general expressions coming from theoretical mechanics. As a collision is a brief event, the particles involved in it represent a closed system. Therefore, the total mass and the momentum are conserved during the collision:

$$m_p + m_t = \sum_i m_i \equiv m_c, \tag{5.11}$$

$$m_p \mathbf{v}_p + m_t \mathbf{v}_t = \sum_i m_i \mathbf{v}_i \equiv m_c \mathbf{v}_c, \tag{5.12}$$

where m_i and $\mathbf{v}_i$ are the masses and velocities of collisional fragments, $\mathbf{v}_c$ is the velocity of their center of mass, and all velocities are in the reference frame of the central body. The kinetic energy before the collision can be expressed through the relative velocity of the colliders, $\mathbf{v}_{\text{imp}} = \mathbf{v}_p - \mathbf{v}_t$, as

$$\frac{1}{2} m_p \mathbf{v}_p^2 + \frac{1}{2} m_t \mathbf{v}_t^2 = \frac{1}{2} m_c \mathbf{v}_c^2 + \frac{m_p m_t}{2 m_c} \mathbf{v}_{\text{imp}}^2, \tag{5.13}$$

but the kinetic energy *after* the collision depends on the physics of the impact that has to be specified.

An approximate, yet reasonably accurate, way to calculate the orbital elements of the fragments is to assert that all of them follow the trajectory of the center of mass: $\mathbf{v}_i = \mathbf{v}_c$ for all i. This implies that all the kinetic energy of the colliders in the center-of-mass reference frame, the last term in Eq. (5.13), is expended in destroying and heating the particles, diminishing the mechanical energy of the cloud of fragments in the reference frame of the primary (*collisional damping*).

We are now able to compute the orbital elements of the fragments a_i and e_i which, as $\mathbf{v}_i = \mathbf{v}_c$, coincide with those of the center of mass, a_c and e_c. By squaring Eq. (5.12) and applying the energy integral we obtain

$$-\frac{G\mathcal{M} m_c}{2a_c} = -\frac{m_p}{m_c}\frac{G\mathcal{M} m_p}{2a_p} - \frac{m_t}{m_c}\frac{G\mathcal{M} m_t}{2a_t} + \frac{m_p m_t}{m_c}\left[\mathbf{v}_p \cdot \mathbf{v}_t - 2\frac{G\mathcal{M}}{r}\right], \tag{5.14}$$

where r is the distance at which the collision occurs. Here, the left-hand side is proportional to the total mechanical energy of the fragment cloud. The expression in brackets depends on the mutual orientation of the p- and t-orbits at the collision point. In the 2D approximation, which is reasonable for a disk with a small semi-opening angle ϵ, the scalar product term is a function of one variable (e.g., the true anomaly of one of the colliders). By letting this variable vary over the admissible range, Eq. (5.14) can be used to find a range of possible semimajor axes $a_c \in [a_{\min}, a_{\max}]$. Taking the cross product of Eq. (5.12) and the radius vector of the collision point, $\mathbf{r}$, results in the conservation law for the angular momentum. Expressing the result through orbital elements, we get

$$m_c\sqrt{a_c(1-e_c^2)} \approx m_p\sqrt{a_p(1-e_p^2)} + m_t\sqrt{a_t(1-e_t^2)}, \tag{5.15}$$

where we have assumed that the average values $\cos i$, $\cos i_p$, $\cos i_t$ are equal, which accounts for the approximate equality sign. Equation (5.15) determines the eccentricity e_c as a function of a_c.

Thus, in the (a, e)-plane, the orbital elements of the collisional fragments form a curve $e_c(a_c)$, extending from $(a_{\min}, e_{\min})$ to $(a_{\max}, e_{\max})$, where $e_{\min} \equiv e_c(a_{\min})$ and $e_{\max} \equiv e_c(a_{\max})$. Examples of these curves for different combinations of parameters are shown in Fig. 8. As expected, when one of the colliders is much heavier than the other, the curves transform to short dashes close to the position of the heavier particle. And vice versa, for equal masses the curves are the longest, indicating an appreciable dispersion of fragments. The resulting a_c's never exceed $\max\{a_p, a_t\}$; the same is true for the e_c's. In some cases either the semimajor axis of some fragments, their eccentricity, or both, are smaller than those of both impactors. This is a clear indication of energy dissipation in the system.

The function $\bar{h}$ we have sought is given by

$$\bar{h}(m, \mathbf{p}) = \bar{h}(m, a, e) = \frac{1}{a_{\max} - a_{\min}} \delta\big[e - e_c(a)\big] H[a - a_{\min}] \times H[a_{\max} - a], \tag{5.16}$$

where H denotes the Heaviside step function equal to 1 for positive arguments and to 0 otherwise, and we have dropped the p- and t-arguments for brevity.

In reality, both a and e are somewhat dispersed around the center-of-mass values, so that the curve $e_c(a_c)$ transforms to an elongated 2D-area. Such a scatter occurs because, although nearly all impact energy goes to comminution and

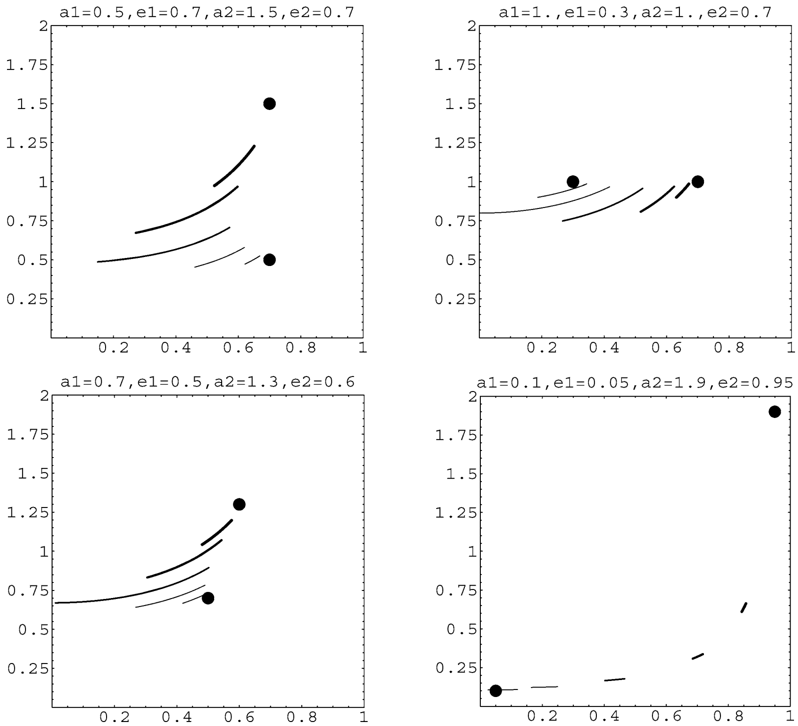

Fig. 8. Orbital elements of two colliding particles and the resulting collisional fragments in the center-of-mass model, depicted in the (e, a)-plane. Different panels are for several combinations of (a, e) of the two colliders, as listed in the legend. The semimajor axis is in arbitrary units. In each panel, two bold dots represent colliders and 5 curves of increasing thickness are collisional fragments for different mass ratios of the colliders: 10, 3, 1, 0.3, and 0.1.

heating, a small fraction still goes to the kinetic energy of the individual fragments. This fraction, that causes relative changes in a and e at each collision, is of the order of a few percent (Fujiwara and Tsukamoto, 1980). If the eccentricities of the particles in a certain system are larger, which they typically are, then the "center-of mass" model is accurate enough. As an exception, we mention planetary rings, where the orbits are nearly circular, so that the scattering effect may cause appreciable, diffusive changes in semimajor axes and eccentricities. The inclination terms (3D corrections) omitted in our analysis of Eqs. (5.14)–(5.15) will cause a similar effect, spreading the fragments over a larger area in the orbital element space. This effect can only be important for disks with large opening angles and is not included in the current model either.

6. Application of the model to the Edgeworth–Kuiper belt

6.1. Objectives

The kinetic model described in the previous sections will now be applied to the collisional evolution of the EKB. Our calculations pursue mostly illustrative purposes: we wish to demonstrate that our model is able to reproduce some salient features of this collisional system found earlier with other methods. We start with an overview of the simplifying assumptions and limitations of our simulations:

- When setting initial conditions, we assume a set of fully formed EKBOs, either in situ (Stern and Colwell, 1997; Kenyon and Luu, 1998, 1999a, 1999b) or transported to the present location by dynamical interactions in the early Solar System (Levison and Morbidelli, 2003). Therefore, we neither endeavor to "build" the early EKB nor find out how the early EKB might look by tracing the evolution backward in time.
- We confine our analysis to the classical, dynamically cold, population of the EKB and do not simulate its collisional interaction with the dynamically hot population (S. Charnoz, personal communication).
- We do not include distant interactions of bodies, especially on crossing orbits (viscous stirring, dynamical friction). because they are not of importance for the (already formed) EKBOs in the size range under study. Indeed, simple estimates that we made on the base of Stewart's stirring equations (see, e.g., Appendix B of Weidenschilling et al., 1997) show that both viscous stirring and dynamical friction, whose timescales are roughly proportional to $(e/s)^3$ (e—orbital eccentricities, s—object sizes), may lead to substantial effects at radii above several hundred km, which we do not consider.
- We ignore cratering impacts, rebounds and merging (Kenyon and Bromley, 2002). Accordingly, we do not touch upon highly debated topics of impact resurfacing and color modification of EKBOs (see, e.g., Thébault and Doressoundiram, 2003, and references therein).

- We do not consider the effects of resonant, secular, and short-period perturbations by giant planets, most notably Neptune, which may substantially modify the distribution and therefore the collisional evolution of the disk (Kenyon and Bromley, 2004b).
- We do not model stochastic fluctuations in the distributions caused by individual collisions of larger bodies (Durda and Dermott, 1997).

Therefore, any conclusions about the real EKB on the basis of these runs should be made with caution. On the other hand, we are not aware of any model that would take into account *all* the effects listed above. Our model provides a better treatment of orbital eccentricities and possible correlations between distributions of masses, semimajor axes, and eccentricities, than other models. Besides, by considering an idealized system it may be easier to reach a better understanding of general properties of EKB-like systems.

6.2. *The collisional code*

The programming implementation of the kinetic model constructed in previous sections is described in Appendix A. We discuss discretization of the phase space, the integration procedure including the stepsize control, and the so-called small size-cutoff problem.

6.3. *Description of the runs*

We considered a system of objects with a bulk density of $1\,\mathrm{g\,cm^{-3}}$ and a mass (size) distribution extending from 10^{-6} g (60 µm) to 10^{23} g (300 km), represented by 45 bins. Of these, the lowest 15 bins (up to 8 kg or the 12 cm radius) were in the smooth exponential cutoff with the control parameter $x = 1.30$ (see Appendix A.2). Thirty "real" bins provided results valid for sizes from about 1 m to 300 km. The mass ratio in successive bins was $\delta_m \approx 4$. We have made tests with a better mass binning ($\delta_m \approx 2$) and found no qualitative differences in any of the distributions that we have analyzed. Quantitative differences were moderate. For instance, the mass density differed by not more than several tens of percent across the whole size range. A similar mass binning has been used in many previous studies: $\delta_m = 4$ (Stern, 1995, 1996), $\delta_m = 3$ (Davis and Farinella, 1997), $\delta_m = 2$ (Stern and Colwell, 1997). The initial mass distribution was taken to be the Dohnanyi power law.

The initial semimajor axis distribution was assumed to be a power law with sharp cutoffs at 30 and 70 AU. As in Stern (1995), two power law indices were used: −2 (for zero eccentricities, it would correspond to the surface mass density proportional to a reciprocal of distance, meaning a constant mass per semimajor axis bin) and −1 (declining mass per semimajor axis bin). The initial eccentricity distribution was uniform between 0.0 and 0.3. When choosing the (a, e)-binning, we kept in mind that, if the (a, e)-grid is too coarse, the fragments may be distributed into the same bins to which

Table 1
Parameters for numerical runs

Run identificator[a]	Initial disk mass [$\mathcal{M}_\oplus$]	Initial slope in $n(a)$	Material
nd-dmb-i	0.33	−2	Ice
nd-dmb-r	0.33	−2	Rock
nd-cmb-i	0.33	−1	Ice
nd-cmb-r	0.33	−1	Rock
ld-dmb-i	0.1	−2	Ice
md-dmb-i	1.0	−2	Ice

[a] md—massive disk, nd—nominal disk, ld—low-mass disk; cmb—constant mass per a-bin, dmb—declining mass per a-bin; i—"ice," r—"rock."

the colliders belong, and the code will fail to simulate possible diffusion-like effects. We have checked that 8 bins in a and 12 bins in e taken in most of the runs were sufficient to avoid missing diffusion due to collisional damping.

The disk was assumed to have a semi-opening angle of 0.3 radians ($\approx 20°$). Three different values of initial total mass of the disk were taken: $1.0\mathcal{M}_\oplus$ (massive disk), $0.33\mathcal{M}_\oplus$ (nominal disk), and $0.1\mathcal{M}_\oplus$ (low-mass disk). We considered both "icy" and "rocky" objects, as described above. The integration interval was 4.5 Gyr in all the cases. The runs are listed in Table 1.

6.4. *Size distribution*

The evolution of the mass distribution in several runs is illustrated by Fig. 9. The upper and lower panels show the distribution at 30 and 70 AU, respectively. Figure 9 demonstrates that, not unexpectedly, a system composed of "icy" objects is eroded more significantly than a similar system of "rocky" bodies. The difference between the runs with a different initial spatial slope (cmb and dmb runs) is only minor.

In agreement with other modeling results and in accord with observations (e.g., Stern, 1995, 1996; Davis and Farinella, 1997; Durda and Stern, 2000; Pan and Sari, 2004), the resulting size distribution is not a Dohnanyi power law. The reason is the size dependence of the fragmentation parameters, most notably the critical specific energy (5.1). The broad dip in the distribution seen at radii of about 0.1 km is a direct consequence of the minimum of $Q_D^*(s_t)$ there (see Fig. 7). This also gives rise to a change in the slope of the distribution at a break radius of several kilometers. The change in the slope, as well as the break radius depend of the critical specific energy, initial disk's mass, and the time elapsed (Pan and Sari, 2004; Kenyon and Bromley, 2004b). A detailed quantitative study of these features in the size distribution and reconciliation with new data on the EKBO size distribution require more realistic modeling, including stirring by Neptune (Kenyon and Bromley, 2004b), which is beyond the scope of this paper.

In is interesting to note that the minimum of $Q_D^*(s_t)$ means that bodies of that size are easier to destroy than the others, which effectively acts as a moderately smooth cutoff for larger sizes. Therefore, we should expect the phenom-

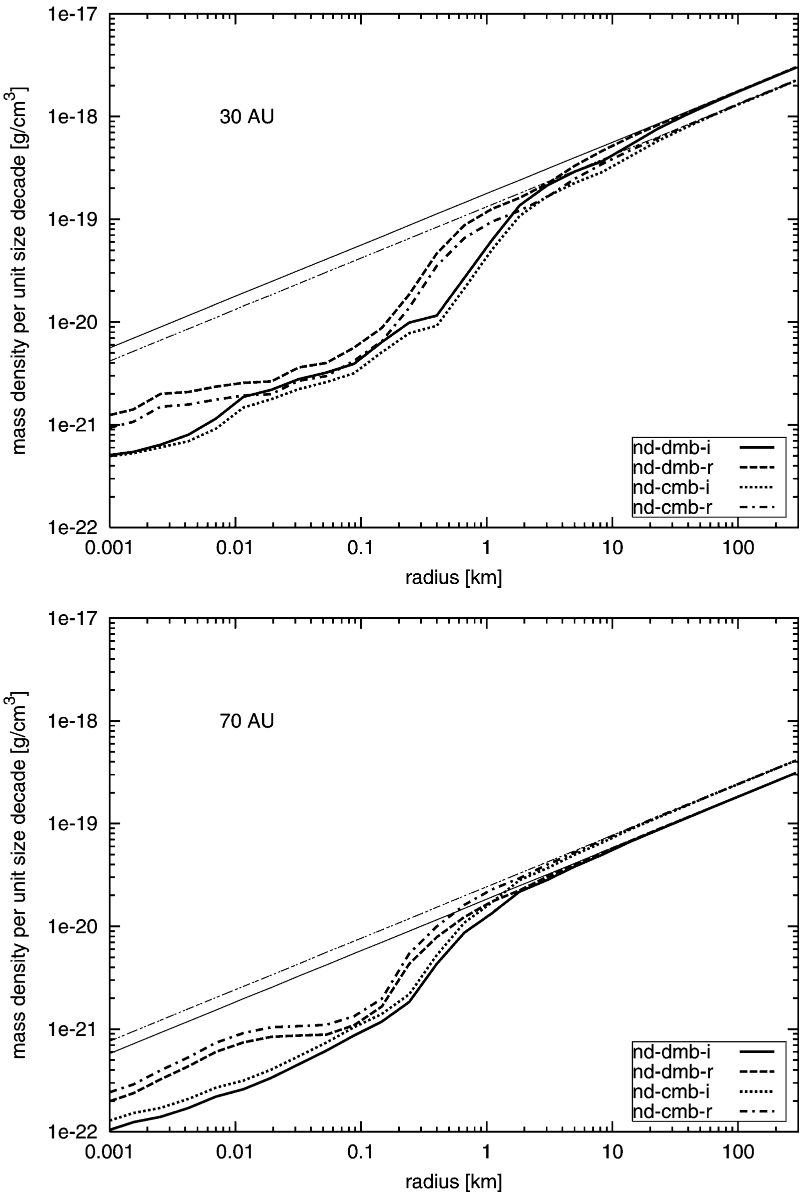

Fig. 9. Size distribution of EKBOs at two different distances from the Sun: 30 AU (top) and 70 AU (bottom). Thin straight lines: initial state, thick curves: final state. Different linestyles are for several runs, which are indicated in the legend and explained in Table 1. To alleviate comparison with other studies, we note that a slope of the differential size distribution is the slope in the figure minus 4. For example, the initial (Dohnanyi's) distributions in our axes have a slope of $+0.5$, which would correspond to a classical index of -3.5.

enon discussed in Appendix A.2—a wavy distribution of bodies above 0.1 km. Indeed, a slight hump is seen in Fig. 9 (top) at several km for ice and at ~ 1 km for rock. What is more, for rock there is a second weak maximum at about ~ 10 km. A similar phenomenon was discussed for the collisional evolution of the asteroidal belt by Durda et al. (1998).

6.5. Collisional lifetime

Figure 10 depicts the average collisional lifetimes as a function of the particle mass—for the initial stage and after 4.5 Gyr. The average lifetimes increase in the course of evolution, following a gradual depletion of the disk. There is a correspondence between the lifetime curves and the mass distribution curves: humps and dips are close to each other (Figs. 9 and 10). This is understandable: maxima in the mass distribution correspond to more abundant particles, and that these are more abundant means that they live longer. The three solid lines of different thickness in each panel are for disks with different initial mass (md-dmb-i, nd-dmb-i, and ld-dmb-i runs). Their comparison confirms that the instantaneous collisional lifetime is inversely proportional the instantaneous disk's mass, as follows directly from Eqs. (3.25)–(3.26).

A look at the absolute values shows that bodies larger that a few km in a 4.5 Gyr-old Kuiper belt must be primordial, whereas smaller ones are most likely fragments from earlier collisions. This falls in agreement with earlier con-

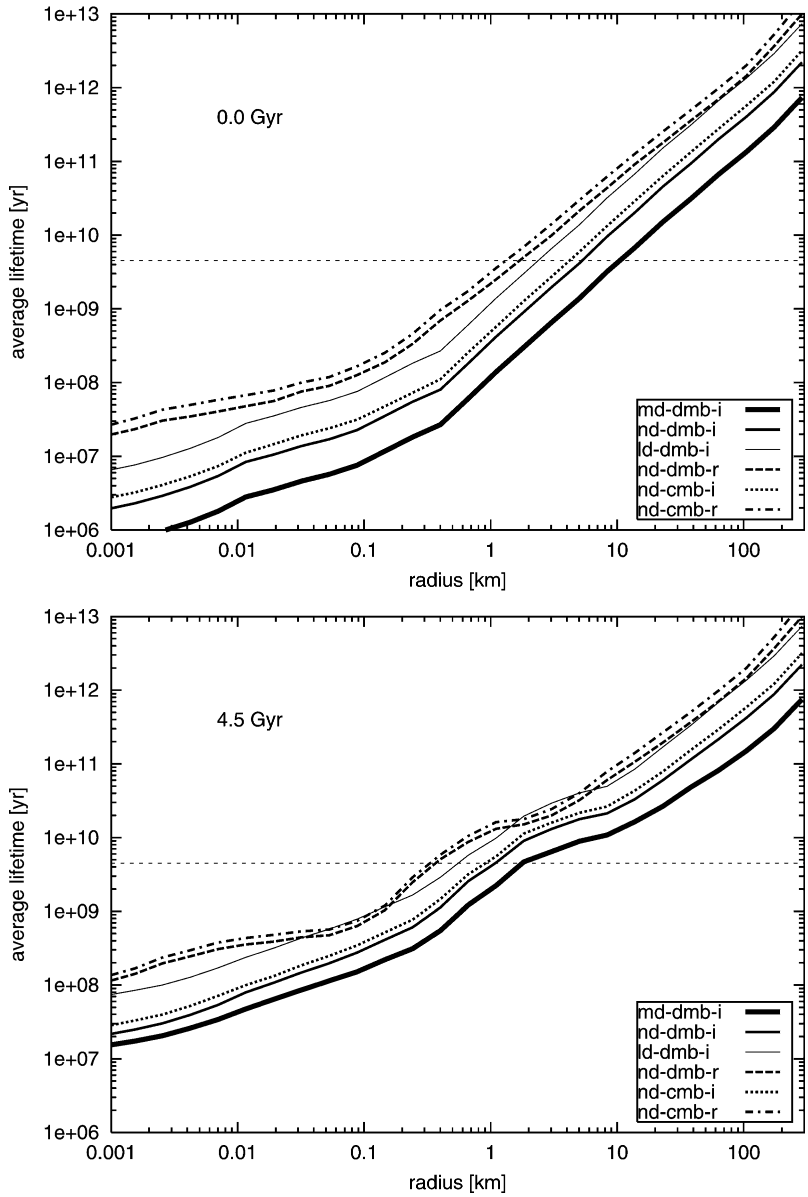

Fig. 10. Average collisional lifetime of different-mass EKBOs, Eq. (3.26): for the initial state (top) and at the final state (bottom). Different lines are for several runs, which are indicated in the legend and explained in Table 1. The integration interval was 4.5 Gyr, and is shown with a horizontal straight line in both panels.

clusions. For comparison, Durda and Stern (2000) found that EKB objects (EKBOs) with $s < 2.5$ km have collisional lifetimes less than 3.5 Gyr, whereas Davis and Farinella (1997) reported several tens of kilometers as the separation size between primordial objects and collisional fragments. Of course, the actual "critical" size depends on a number of model parameters—for instance, on mechanical properties of EKBOs. For larger, 100 km EKBOs Durda and Stern (2000) found the destruction time to range from 3×10^{12} to 8×10^{12} years, which is in a good agreement with our results, too. Kenyon and Bromley (2004b, their Fig. 2) report values close to ours for ~ 1 km objects, but much shorter timescales for smaller EKBOs and much longer for larger ones. The difference for small objects traces back to their much larger disk's mass of $10 M_{\oplus}$ at the initial moment to which their removal timescales refer. For larger EKBOs, the difference is probably due to the fact that Kenyon and Bromley include accretion (their Eq. (10)), while we do not.

6.6. Mass loss

We have also traced the collisional mass loss by the Kuiper disk. Recall that in our model the mass is lost through small collisional fragments whose masses fall into bins $im < N_{cb}$, see Appendix A.2. Figure 11 shows that the mass loss rate is very high at the initial phase of evolution and slows down as the disk mass decreases. The mass loss rate is higher for more massive disks. During 4.5 Gyr, the disks with initial masses from $0.1\mathcal{M}_{\oplus}$ to $1.0\mathcal{M}_{\oplus}$ lost 6 to 13% of their

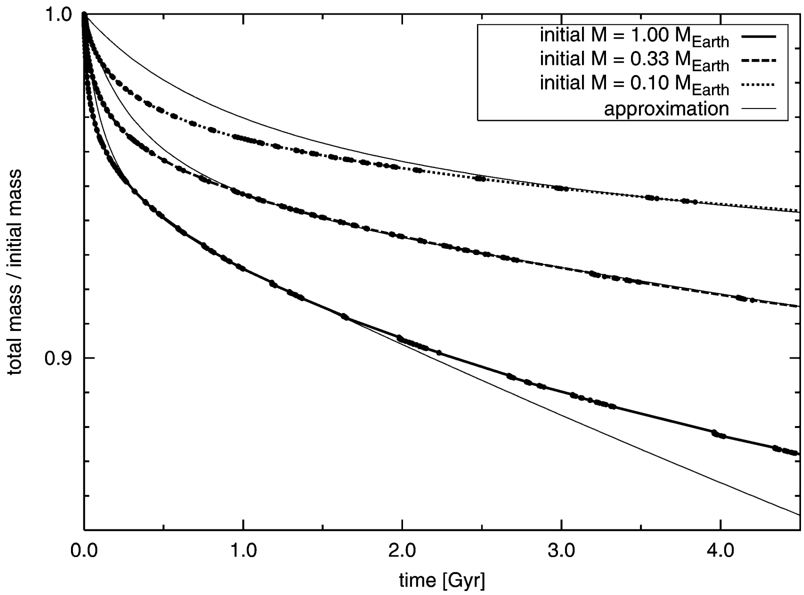

Fig. 11. Mass loss by the Kuiper disk for the md-dmb-i, nd-dmb-i, and ld-dmb-i runs (thick lines). Bold dots on the curves show integration steps assigned automatically on the base of Eq. (A.4) with $\delta = 0.1$ (typically 100—300 in total, depending on the run). Thin solid lines depict the solution of Eqs. (6.1)–(6.3) with constants found from fitting of the middle curve.

initial mass, of which a half occurred during the first 0.5 to 1 Gyr.

We now seek a qualitative explanation of these results from a simple physical argument. We try a rough two-component model that includes populations of "large" objects with total mass $M_L(t)$ and "small" ones with mass $M_S(t)$, so that the total disk mass is $M(t) = M_L(t) + M_S(t)$. Each population is assumed to gradually erode by mutual collisions. Simultaneously, small objects are gained as fragments of collisions of large objects. These processes are described by differential equations

$$\dot{M}_L = -C_L M_L^2, \tag{6.1}$$

$$\dot{M}_S = +C_L M_L^2 - C_S M_S^2, \tag{6.2}$$

where C_L and C_S are positive constants. The right-hand side terms are quadratic in mass, because our basic equations (3.24)–(3.25) are quadratic in the phase space distribution n. Next, denote by M_0 the initial mass of the disk (at $t = 0$) and by f $(0 < f < 1)$ the initial fraction of mass in large objects. Thus the initial mass of large and small objects is

$$M_L(0) = f M_0 \quad \text{and} \quad M_S(0) = (1 - f) M_0. \tag{6.3}$$

Equations (6.1) and (6.2) with initial conditions (6.3) allow an analytic solution in a closed form, but the solution is rather lengthy and is therefore not shown here. We used it to fit the middle curve in Fig. 11 (the nominal value of the initial mass, $0.3\mathcal{M}_\oplus$) and to determine the constants: $f = 0.93$, $C_L = 0.024\mathcal{M}_\oplus^{-1}\,\mathrm{Gyr}^{-1}$, and $C_S = 101\mathcal{M}_\oplus^{-1}\,\mathrm{Gyr}^{-1}$. Then we applied the solution, without changing the constants, to two other curves. The results are also shown in Fig. 11. Our simple model provides a reasonably good scaling of the mass loss rate for different values of M_0. Besides, it explains the high mass loss rate during the first Gyr and the nearly constant one after that: the mass is lost rapidly until the population of small bodies is appreciably depleted and the loss and gain terms in Eqs. (6.1) and (6.2) come to balance. At that stage, the absolute mass loss rate $C_L M_L^2 \approx C_L M_0^2$ ranges from $2 \times 10^{-4} M_\oplus\,\mathrm{Gyr}^{-1}$ (ld-dmb-i run) to $2 \times 10^{-2} M_\oplus\,\mathrm{Gyr}^{-1}$ (md-dmb-i). Of course, this is less than the *average* mass loss rate of 1×10^{-3} to $3 \times 10^{-2} M_\oplus\,\mathrm{Gyr}^{-1}$ for the same runs.

It is interesting to compare our mass loss model with that of Dominik and Decin (2003). They used a similar approach to describe collisional removal of planetesimals that act as sources of circumstellar dust in Vega-type systems, in an attempt to explain the observed decay of debris disks with stellar age. They used a simpler, one component model equivalent to our Eq. (6.1) which, as pointed above, is a good approximation after the initial rapid removal of smaller planetesimals. Thus our results, confirming the conclusion of a nearly constant mass loss rate at later stages (see also, Kenyon and Bromley, 2004a), can serve as an extension of their model to earlier stages of the disk evolution.

6.7. *Spatial distribution*

The same runs allow us to trace the evolution of the spatial distribution in the disk. Figure 12 shows the surface mass density profile for two models and two moments in time—the initial one and after 4.5 Gyr of evolution. As expected, the innermost part of the disk gets progressively depleted. This reflects the fact that the disk is denser towards the Sun and the collision velocities are larger there, so that the collisional evolution is more intensive in the inner region. This agrees with other studies (see, e.g., Davis and Farinella, 1997).

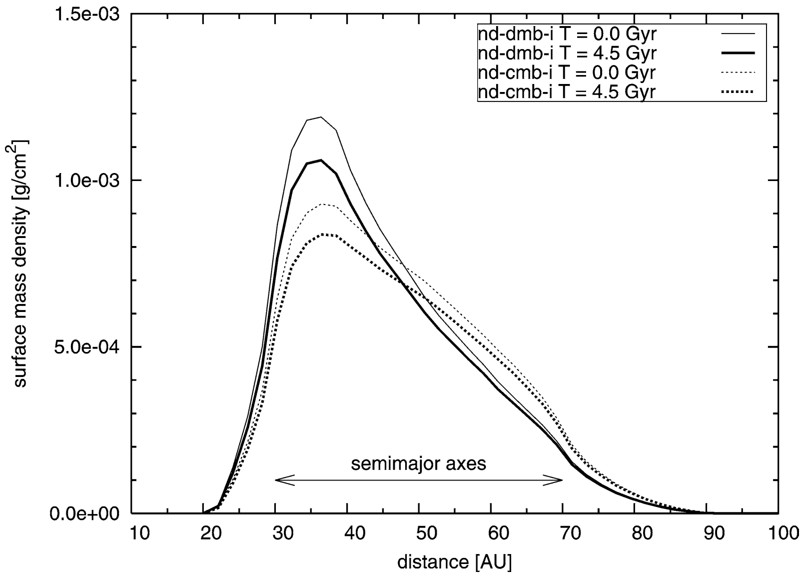

Fig. 12. Evolution of the spatial distribution in the disk with time: surface mass density (Eq. (2.24)) as a function of heliocentric distance. Shown are the results of two runs with different initial slope of $n(a)$: declining mass per a-bin (solid line) and constant mass per a-bin (dotted line). The double-headed arrow marks the range of semimajor axes adopted.

6.8. *Distribution of orbital elements*

We now look at the evolution of the full phase space distribution of the Kuiper belt objects, which is perhaps the most interesting part of the analysis, because it is concerned with the combined evolution of all three phase space variables; mass, semimajor axis, and eccentricity. For illustrative purposes, we have chosen one of the runs, namely nd-cmb-i —a disk with "nominal" mass, initially constant mass per a-bin, and icy objects. The results are shown in Figs. 13–14. Each panel presents a distribution of objects in the (e, a)-plane. The left-hand columns of either figure depict the total *mass* of the objects in different (e, a)-bins and the right-hand columns show the total *number* of objects.

Figure 13 presents the phase space distributions of large objects (bins 38–43, radii 14–170 km). From top to bottom, we plot the (e, a)-distribution of objects for different instants in time, starting from the initial state and ending at 4 Gyr. The grey scale is fixed through each vertical column of panels. The uppermost panels are uniformly black. The uniformity reflects the facts that in a cmb-run both the total masses and numbers of objects in all a-bins are initially the same, and that our initial e-distribution is also uniform. That the uppermost panels are black means that the total mass and number of objects are maximum at the beginning. It is due to the fact that the EKB is not replenished, and the loss terms supersede the collisional gain terms. The middle and lower panels all show that the collisional erosion leads to the formation of a clear V-shape pattern: the bins with largest a and intermediate e retain the largest amount of material, whereas the bins with smallest a and both low and high eccentricities are the most depleted. In Appendix B we describe a series of numerical tests and provide an explanation of the effect. Namely, we show that enhanced depletion at smaller a simply reflects more intensive collisional evolution closer to the Sun, whereas predominant depletion at both smaller and higher e stems largely from collisional probabilities between objects with different orbital eccentricities.

Figure 14 shows the distribution of smaller bodies (bins 19–23, radii 1–7 m), but the panels from top to bottom have a different meaning than in Fig. 13. Instead of showing black rectangular areas as in Fig. 13 (top), we put in the upper panels the state of the system right after the evolution started, at $t = 4$ Myr. These panels illustrate the rapid depletion of small objects at the early stage of the evolution and formation of the V-shape patterns discussed above. These patterns are still present after 4 Gyr of the evolution (Fig. 14 (middle)). Note that the linear grey scale in the upper and middle panels is now different. Finally, the lowest panels are the same as the middle ones, but drawn in the log scale. This scale "overexposes" the region $a \geqslant 30$ AU, but makes visible a new row of filled bins at a between 25 and 30 AU. These bins, whose density increases towards smaller eccentricities, arise from the collisional damping (see Section 5.4 and Fig. 8) that gradually relocates the material to regions with smaller a and e. The binary collision model of Section 5.4 also ensures that initially empty bins with $e > 0.3$ and/or $a > 70$ AU do not get filled.

There are a number of other features seen in the figures. For instance, a comparison of Figs. 13 and 14 shows that the population of meter-sized objects is depleted to a much higher degree than that of the largest bodies. In fact, most of the largest, 100 km-sized bodies beyond ≈ 50 AU still remain intact over several Gyr of collisional evolution.

The phase distributions for the other runs listed in Table 1, not shown here, allow a similar interpretation. For instance, the dmb-runs where the low-a bins initially contain more

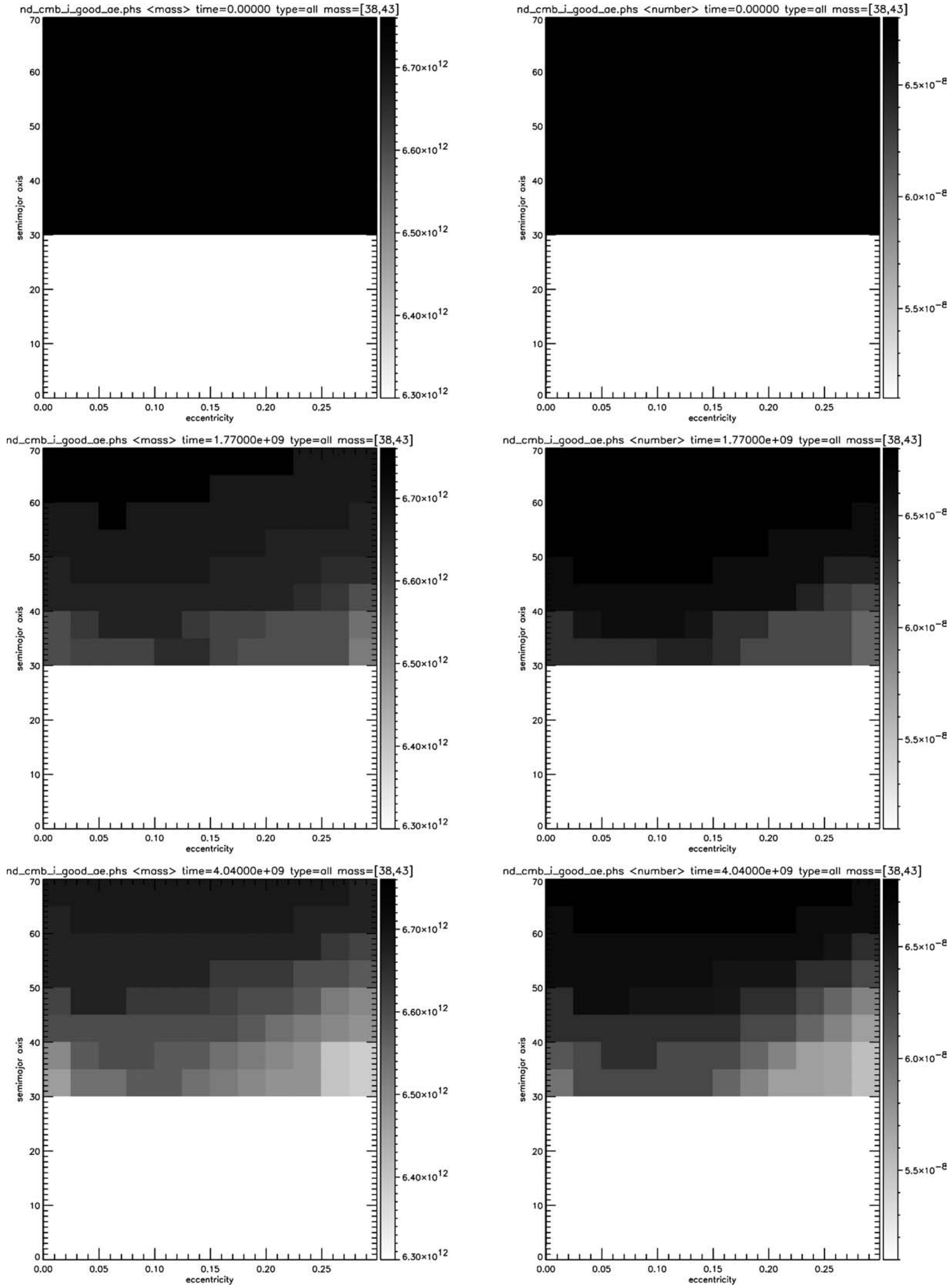

Fig. 13. Distribution of large (14–170 km-sized) objects in the eccentricity–semimajor axis plane (12 bins in e and 8 bins in a). (Left) Total mass of particles. (Right) Total number of particles. (From top to bottom) System's state at $t = 0.0$, 1.8, and 4.0 Gyr. The grey scale used in all panels is linear and is the same for all panels of either column.

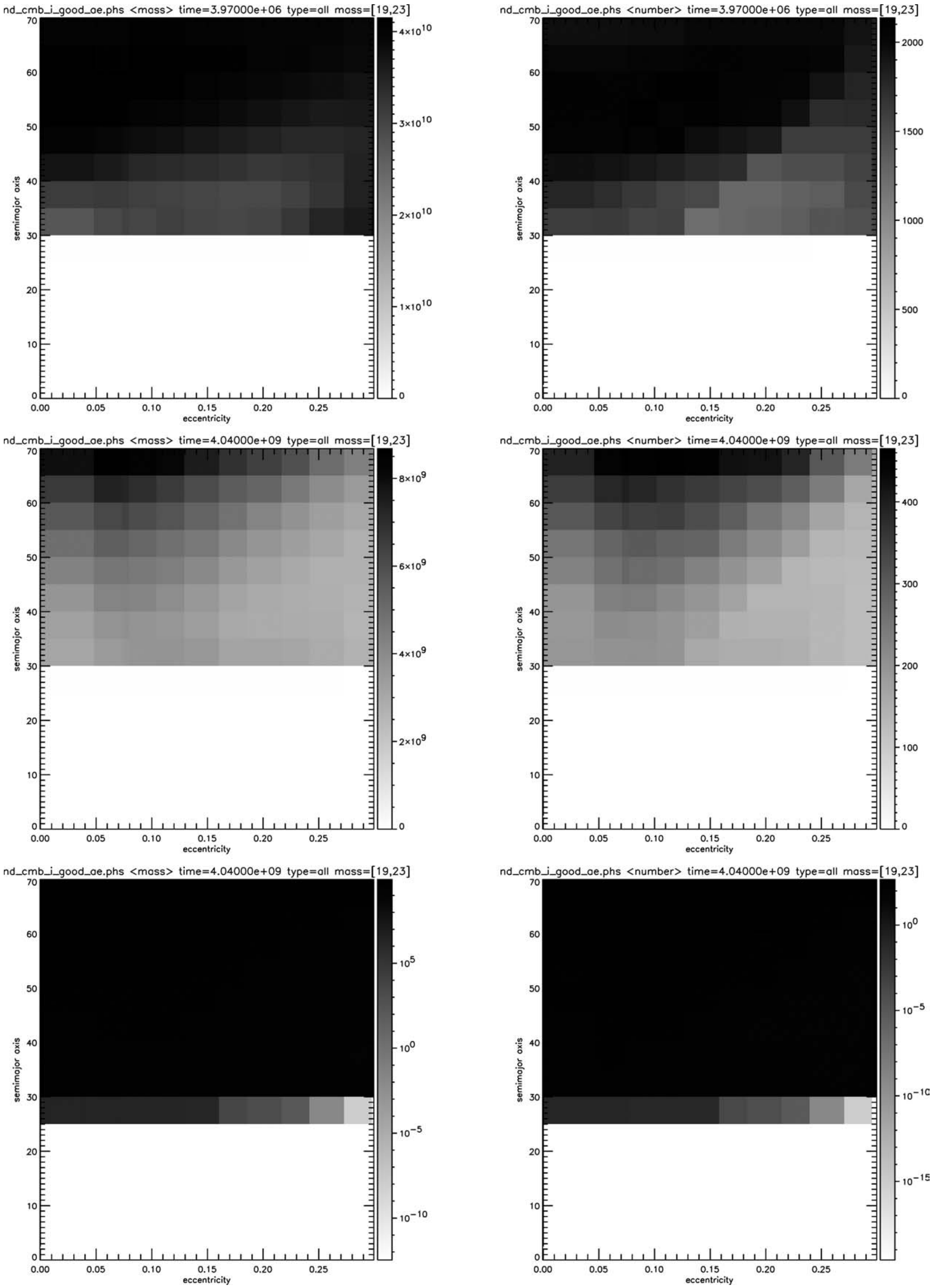

Fig. 14. Similar to Fig. 13, but for small (1–7 m-sized) objects. (Top) $t = 4$ Myr, (middle and bottom) $t = 4.0$ Gyr (linear and log grey scale, respectively).

material than the high-a bins, yield X-shape rather than V-shape distributions: bins with low a, regardless of e, still contain a lot of objects after 4.5 Gyr—because they were quite dense initially.

6.9. Velocity distribution

We finally look at the evolution of the velocity distribution. The results for the same nd-cmb-i run that we have chosen in the previous section are shown in Fig. 15. The left and right panels correspond to upper and low mass bins used in Figs. 13 and 14, respectively. Each panel depicts the initial and final distributions of two velocity components, radial v_r and azimuthal v_ϕ, for a fixed heliocentric distance of 45 AU. Both components are scaled to the circular Keplerian velocity $v_{\rm circ} = \sqrt{G\mathcal{M}/r}$. Besides, $v_{\rm circ}$ is always subtracted from v_ϕ. Lines show marginal distribution of v_r and v_ϕ separately, whereas insets contain 2D plots of $n(v_r, v_\phi)$. Isolines in the insets are close to ellipses with a classical ratio 2:1 (see, e.g., Lissauer, 1993). The smallest ellipses, looking like black spots, correspond to ($v_r \approx 0$, $v_\phi \approx v_{\rm circ}$) and therefore to $e \approx 0$. Larger ellipses correspond to higher e, and are getting increasingly distorted. The complete grey "ellipse" is a transformation of the shaded area in Fig. 2 weighted by the jacobian, Eq. (2.10).

An inspection of Fig. 15 reveals some of the effects discussed before:

(1) The largest effect is a substantial depletion of small particles: the difference between the initial and final states in the right panel is much larger than in the left panel.
(2) Another effect is a stronger depletion of the inner rings, i.e., a preferential loss of particles with smaller a and consequently, with $v \approx v_\phi < v_{\rm circ}$. This is seen as the slight left-right asymmetry of dashed lines in the left panel ($v_\phi - v_{\rm circ} < 0$ versus $v_\phi - v_{\rm circ} > 0$).
(3) A V-shape pattern that appears in Figs. 13 and 14 should correspond roughly to a smaller depletion of the middle-sized ellipses. The effect is difficult to spot, but it is still visible in the right panel for the smaller masses, both in the lines and insets.

7. Summary and discussion

7.1. Model

In this paper we have employed the kinetic theory of statistical physics to describe a disk of solid particles orbiting a primary and experiencing inelastic collisions. As distinct from other collisional models that use a 2D (mass–semimajor axis) binning and perform a separate analysis of the velocity (eccentricity, inclination) evolution, we choose mass and orbital elements as independent variables of a phase space. The distribution function in this space contains full information on the combined mass, spatial, and velocity distribution of particles. General kinetic equations for the

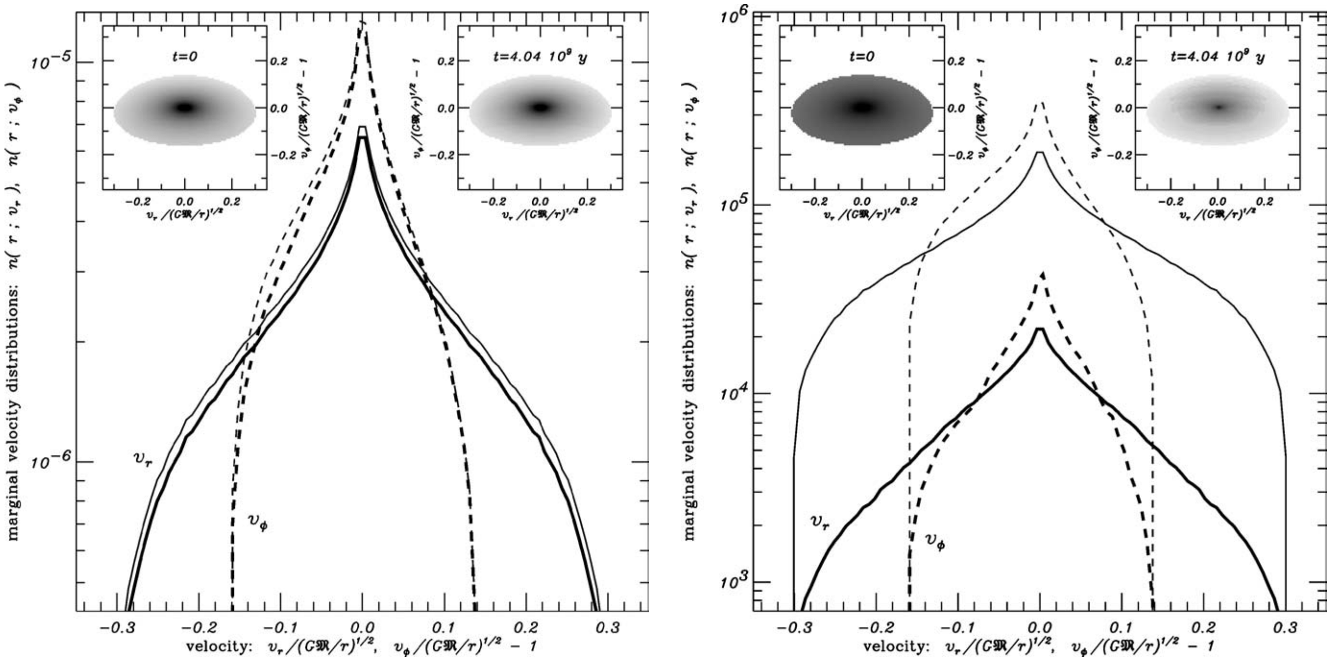

Fig. 15. Velocity distribution $n(\mathbf{r}, \mathbf{v})$, Eq. (2.10), for the nd-cmb-i run. Shown are distributions of the radial and azimuthal velocity components at a distance $r = 45$ AU from the Sun, both in units of the circular Keplerian velocity $v_{\rm circ}$ at that distance. (Left) Large (14–170 km-sized) objects, (right) small (1–7 m-sized) objects. (Lines) Marginal distributions of v_r (solid) and v_ϕ (dashed), obtained by integration over the other component. (Insets) 2D distributions $n(v_r, v_\phi)$. of v_r and v_ϕ. (Thin lines and left insets) Initial state, (thick lines and right insets) final state. The vertical axis for lines and the grey scale for insets are logarithmic.

distribution function (Eqs. (3.23)–(3.25)) are derived. These are valid for any set of orbital elements **p** and for any collisional outcome, specified by a single kernel function f.

The first implementation of the model devised here uses $\mathbf{p} = (a, e)$, i.e., a mass–semimajor axis–eccentricity phase space, and involves averages over the inclination and all angular elements. We assume collisions to be destructive, simulate them with available material- and size-dependent scaling laws, and include collisional damping. A closed set of kinetic equations for a mass–semimajor axis–eccentricity distribution is written and transformation rules to usual mass and spatial distributions of the disk material are obtained.

7.2. *Application to the EKB*

As an application of the model, we have studied the collisional evolution of the classical population in the Edgeworth–Kuiper belt (EKB). We ran the model for different initial disk masses and radial profiles and for objects with different impact strengths. Our results for size distribution, collisional timescales, and mass loss fall in agreement with previous studies. In particular, the collisional evolution is found to be most substantial in the inner part of the EKB. In that region, the separation size between the objects that have survived intact over the EKBs age and those that represent remnants of earlier collisions lies between a few km and several tens of km. The size distribution in the EKB is not a single Dohnanyi-type power law and reflects the size dependence of the critical specific energy in both strength and gravity regimes. In accord with other studies, the net mass loss rate of an evolved disk in nearly constant and is dominated by disruption of larger objects. Finally, assuming an initially uniform distribution of orbital eccentricities, we have shown that an evolved disk contains more objects in orbits with intermediate eccentricities than in near-circular and more eccentric orbits. This property holds for objects of any size and is explained in terms of collisional probabilities. The effect should modulate the eccentricity distribution shaped by dynamical mechanisms, such as resonances and truncation of perihelia by Neptune.

7.3. *Limits of the present model and its possible extensions*

As with any model of a complex system, it is important to understand both the validity limits of the approach and the degree of fidelity of the current implementation. We distinguish between principal limitations and those that can be relaxed. The assumptions of the first kind are that: (i) the system is not too dense to ensure that finite-size effects are absent, packing factor is negligible, triple and multiple collisions are unimportant etc.; (ii) no energy is partitioned into rotational degrees of freedom of the objects; (iii) the largest bodies considered are still numerous enough to be represented by a continuous distribution, which is a principal limitation inherent to the coagulation equation. The assumptions of the second kind are as follows: (1) the inclination distribution does not evolve with time; (2) apsides and nodes of particles' orbits are distributed uniformly and therefore, the disk is rotationally symmetric; (3) between collisions, all grains move in Keplerian orbits; (4) these orbits are bound, i.e., elliptic; (5) long-range interactions (dynamical friction, viscous stirring etc.) are absent; (6) collisions lead to full destruction of both colliders and generation of smaller debris; (7) there is no direct supply of material into the system.

Assumptions (1)–(2) can, in principle, be lifted by adding inclination and/or angular elements to the list of phase space variables and by treating them in the same way as semimajor axis and eccentricity. This step is straightforward as far as derivation of formulas is concerned, but would result in a model very demanding to the computer resources. We estimate that adding one more variable, namely the inclination, would still yield a model that delivers results in reasonable times. For smaller objects with collisional timescales less than the integration time, a model with a, e, i as phase space variables would, of course, reproduce an approximate equipartition of energy and the resulting coupled evolution of distributions of e and i. In particular, a classical relation $\langle i\rangle/\langle e\rangle \sim 0.5$ (e.g., Greenberg et al., 1991) would be expected.

In contrast, lifting assumptions (3)–(7) would require additional math effort, but would not pose any severe computational limitations. Here we sketch some of the possibilities. One can generalize the master equation (3.23) by including an additional diffusion term:

$$\frac{\partial n}{\partial t}(m, \mathbf{p}) = \frac{dn}{dt}(m, \mathbf{p}) - \frac{d\mathbf{p}}{dt} \cdot \frac{\partial n}{\partial \mathbf{p}}(m, \mathbf{p}), \qquad (7.1)$$

where dn/dt is given by Eq. (3.23) and $d\mathbf{p}/dt$ is the time derivative of the vector of orbital elements **p**, assumed to evolve under perturbing forces. This offers a way to include drag forces and gravitational perturbations by large bodies in the disk, including resonant cases. One simply takes $\mathbf{p}(t)$ from known solutions of the perturbation equations of celestial mechanics that give osculating or mean elements as functions of time. The same applies to the dynamical friction and viscous stirring: equations for $\mathbf{p}(t)$ provided, e.g., by Stewart and Ida (2000) can be used. Direct radiation pressure can be included through the usual formalism—the gravitational problem with a reduced central mass (Burns et al., 1979). For dust-sized particles, one has to allow them to move in unbound orbits (Krivov et al., 2000). This does not imply any changes in the basic equations (3.23)–(3.25) but does require, above else, generalization of transformation formulas (e.g., Eqs. (2.10), (2.18), (3.29)–(3.30)) to the hyperbolic case. A way to include further collisional outcomes — cratering, restitution, agglomeration—is to adjust the fragment-generating function f (see Eq. (3.8) and a discussion there). Finally, replenishment of material from physical sources can be simulated by adding supply terms to Eq. (3.23) or Eq. (7.1).

We believe that future work on these issues will be rewarding. Potential applications are many and, besides the

EKB, may include protoplanetary disks, the main asteroid belt, zodiacal cloud, circumstellar debris disks, and planetary rings.

Acknowledgments

We thank Sébastien Charnoz and the anonymous referee for thorough and extremely speedy reviews that helped to significantly improve the manuscript and Jim Howard for stylistic improvements. This work was partly funded by Deutsches Zentrum für Luft- und Raumfahrt (DLR), project 50 OH 0003, and by Deutsche Forschungsgemeinschaft (DFG), projects Sp 384/12-1 and Kr 2164/1-2.

Appendix A. Implementation of the model

A.1. Numerical solution of the kinetic equation

First we discretize the kinetic equation (3.23) by introducing a mesh in variables m, a, and e and replacing integration with summation over discrete values m_{im}, a_{ia}, and e_{ie}. The kinetic equation (3.23) with the gain term (3.24) and loss term (3.25) are integrated with a first-order Euler routine to find the phase space distribution $n(m_{im}, a_{ia}, e_{ie})$ at different instants of time. It means that, on the base of the equation,

$$\frac{dn}{dt}(m_{im}, a_{ia}, e_{ie}) = \left(\frac{dn}{dt}\right)_{\text{gain}}(m_{im}, a_{ia}, e_{ie}) - \left(\frac{dn}{dt}\right)_{\text{loss}}(m_{im}, a_{ia}, e_{ie}), \tag{A.1}$$

the state of the system $n_{i+1}(m_{im}, a_{ia}, e_{ie})$ at time $t_{i+1} = t_i + \Delta t$ is found from the state $n_i(m_{im}, a_{ia}, e_{ie})$ as

$$n_{i+1}(m_{im}, a_{ia}, e_{ie}) = n_i(m_{im}, a_{ia}, e_{ie}) + \Delta n_i(m_{im}, a_{ia}, e_{ie}), \tag{A.2}$$

where

$$\Delta n_i \equiv \left(\frac{dn_i}{dt}\right)(m_{im}, a_{ia}, e_{ie})\Delta t. \tag{A.3}$$

The best strategy is to use an adaptive step size. Most "dangerous" are large negative increments of n which, for too large Δt, can make $n(m_{im}, a_{ia}, e_{ie})$ for some of the indices negative, causing numerical instabilities. We therefore require that

$$\max_{im,ia,ie \text{ such that } n_i \neq 0 \text{ and } \Delta n_i < 0} \left|\frac{\Delta n_i(m_{im}, a_{ia}, e_{ie})}{n_i(m_{im}, a_{ia}, e_{ie})}\right| \leqslant \delta, \tag{A.4}$$

where $0 < \delta < 1$ is an input parameter. We take $\delta = 0.1$. Inequality (A.4) is used to dynamically set the "new" step size Δt before a current time step is completed. As a check for numerical stability of solutions, we inspect the maximum absolute value of the relative increment of *any* sign,

$$\max_{im,ia,ie \text{ such that } n_i \neq 0} \left|\frac{\Delta n_i(m_{im}, a_{ia}, e_{ie})}{n_i(m_{im}, a_{ia}, e_{ie})}\right|, \tag{A.5}$$

and typically see that these quantities, being large at the beginning of integration, gradually tend to δ, indicating a dynamical balance between the sources and losses.

Once the phase space distribution $n(m_{im}, a_{ia}, e_{ie})$ for a certain moment of time is found, it is converted into the mass-distance distribution $N(m, r)$ with the aid of Eq. (2.18) or Eq. (2.22). In our code, the integrals (2.18) and (2.22) are evaluated by a Monte Carlo method which helps maintain high precision close to the singularity $a(1-e) = r$. Further quantities, such as the mass density distribution (2.23) and surface mass density (2.24), are also calculated.

A.2. The small-mass cutoff problem

In his fundamental work, Dohnanyi (1969) considered a closed system with destructive collisions, assuming two important conditions: (i) the mass range extends from zero to infinity, and (ii) fragmentation parameters are independent of particles' mass. He has shown that the mass distribution in such a system relaxes to a single power law

$$n(m, a, e) \propto m^{-p} \tag{A.6}$$

with the index $p = 11/6 = 1.83\ldots$. In reality, neither condition is fulfilled, however. First, the small-mass end of the mass distribution usually represents a "channel" through which the material is lost by the system: at least at dust sizes, the particles are vulnerable to radiation pressure, plasma drag forces, and erosion or sputtering processes which start to determine their lifetimes instead of collisions. Second, the fragmentation parameters do depend on the particle sizes: for instance, the critical energy does. What is more, condition (i) introduces a serious problem into the simulations. Indeed, any modeling assumes a certain minimum mass (or size), below which the particles are simply ignored.

Campo Bagatin et al. (1994) showed that the presence of a small-size cutoff makes a mass distribution wavy. In Fig. A.1 (dash-dotted line) we show such a wavy distribution for a Kuiper belt-like system where we assumed a constant $Q_D^* = 3 \times 10^6\ \text{erg}\,\text{g}^{-1}$ over the whole mass range and $c = 1.24$ (see Section 6.3 for other details about the parameters adopted). A wavy structure, superimposed on the Dohnanyi's equilibrium slope, arises because particles with sizes just above the cutoff are not eliminated by smaller projectiles (which are absent) and therefore are produced by break-up of larger bodies faster than they are removed. Consequently, larger particles are increasingly depleted up to the mass where the smaller stuttering impactor exceeds the cutoff. Beyond then, the removal rate is reduced and the distribution flattens. The pattern then reproduces itself at larger and larger masses.

It is important to understand that the wavy pattern is not an artefact of the modeling, but an intrinsic property of a system with a small-mass cutoff. Campo Bagatin et al. (1994)

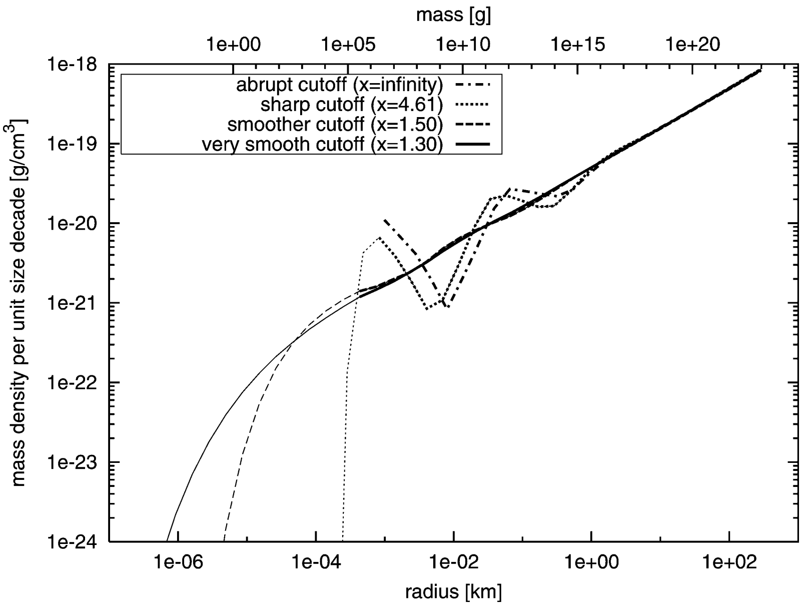

Fig. A.1. Typical size distributions under different assumptions about the small-size cutoff. Plotted is the mass density per unit logarithmic size interval (Eq. (2.23)) as a function of size. The region of the cutoff itself is shown with a thin line. The cutoff parameters are shown in the legend. The smoother the cutoff, the less wavy the distribution.

have shown that the amplitude of the wave depends on how abrupt the cutoff is, and that the wavelength depends on the mechanical properties of the bodies. They pointed out that the wave does not develop if the effective width of the cutoff exceeds the wavelength.

Although a possibility that the behavior of smallest, dust-sized debris may affect the size distribution of large asteroids and EKBOs cannot be completely ruled out, we argue that it does not seem likely. Let us see, for instance, what happens with particles of smaller and smaller size. Starting from the radius of about $\sim 10^2$ µm, for which the Poynting–Robertson lifetimes become comparable to the collisional ones, the Poynting–Robertson lifetimes of meteoroids become increasingly shorter. This takes place until the radii reach ~ 1 µm, at which size the direct radiation pressure becomes comparable in strength with the solar gravity, changing the dynamics and distributions again. Consequently, there must exist a “Poynting–Robertson cutoff” extending over 2 orders of magnitude in terms of sizes, or 6 orders of magnitude in terms of mass. This exceeds the typical wavelength and therefore makes the cutoff smooth enough to prevent formation of the wave. Thus we are left with a merely technical problem: how to avoid triggering of the wave in the simulations without extending the modeling to the dust sizes.

The issue was analyzed in depth by Durda and Dermott (1997) who suggested using an artificial smooth cutoff below the mass range of interest. We now describe their (slightly modified) technique implemented in our model. All mass bins, with indices $im = 0, \ldots, N_m$, are divided into two parts. Upper mass bins, from a certain N_{cb} to N_m, are treated as “real” bins that cover the mass range of interest. Lower mass bins, $im = 0, \ldots, N_{cb} - 1$, are declared “cutoff” bins,

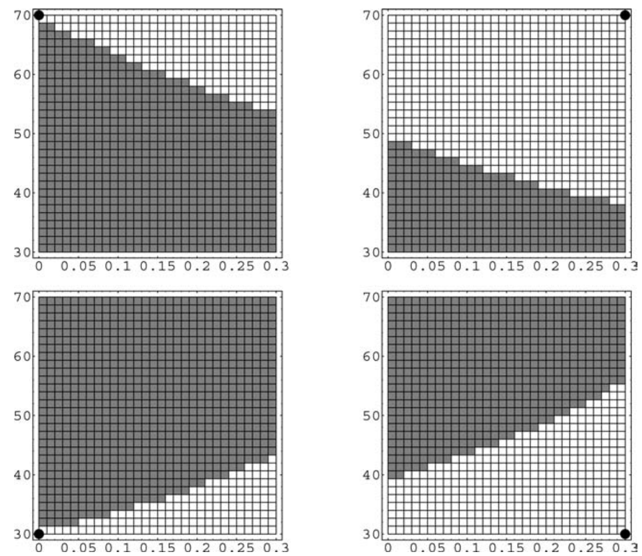

Fig. B.1. The eccentricity–semimajor axis mesh. Unshaded region represents the orbits that intersect a given orbit (bold dot). Four panels are for different positions of the latter.

and are only introduced to smoothly fade the distribution. The phase space density in these cutoff bins is calculated as

$$n(im) = \text{extrapolation}(im) \cdot \text{scaling}(im), \tag{A.7}$$

where extrapolation(im) is $n(im)$ computed by extrapolating the two lowest “real” bins with indices N_{cb} and $N_{cb} + 1$ to the bin with index im, and scaling(im) is a decay factor,

$$\log_{10}\bigl[\text{scaling}(im)\bigr] = \frac{1}{10}\bigl(1 - x^{N_{cb} - im}\bigr) \tag{A.8}$$

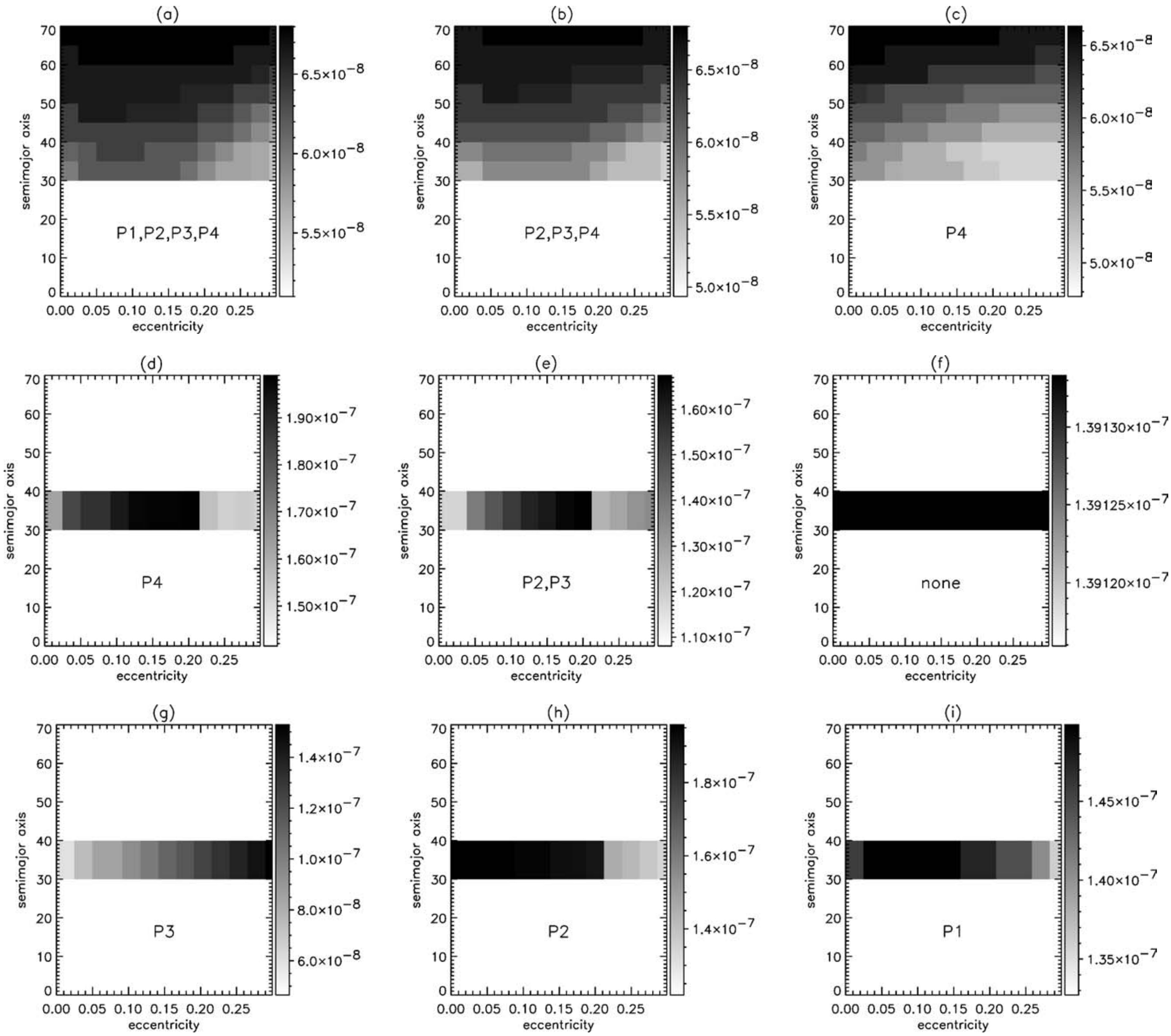

Fig. B.2. Results of numerical runs made to explain the "eccentricity effect." See text for description of the panels.

with $x \geqslant 1$ being a parameter that controls the strength of the cutoff ($x = 1$, no cutoff; $x \to \infty$, an abrupt cutoff). Several lines in Fig. A.1 show the size distribution of one and the same system with different cutoff parameters—from $x \to \infty$ (abrupt cutoff) to $x = 1.30$ (corresponds to $n(N_{cb})/n(0) = 10^5$ and $m(N_{cb})/m(0) = 10^{11}$, i.e., to a phase space density drop by 5 orders of magnitude over 11 orders of magnitude in mass). The smoother the cutoff, the less wavy the distribution. The smoothest cutoff gives a wave-free Dohnanyi distribution (solid line).

Appendix B. Non-uniformity of the e, a-distribution

Here we discuss the V-shape patterns seen in Figs. 13–14. The essence of the effect is that a collisionally evolved disk, whose (e, a)-distribution was initially uniform, contains more objects with largest semimajor axes and intermediate eccentricities, whereas the objects with smallest a and both low and high e are the most depleted.

We can decompose the effect into the following two: (i) bins with smaller a are more depleted, and (ii) bins with both smaller and larger e are more depleted that those with intermediate e. The effect (i) is trivial: both the number density of objects and impact velocity increase towards smaller a, so the intensity of collisional processes is higher closer to the Sun. It remains to explain the "eccentricity effect" (ii). To this end, we look at the kinetic equations (3.23)–(3.25) and at the integration limits in those. There are four eccentricity-dependent places there, which can do the job:

(P1) The function $\bar{f}$ in the gain term that describes generation of collisional fragments. One can expect that the "center-of-mass" model of Section 5.4 tends to choose e of collisional fragments between those of two colliding particles, thereby "preferring" intermediate values of e.

(P2) The impact velocity $\overline{v_{\text{imp}}}$ grows with eccentricities of colliders (see Fig. 6), favoring removal of objects in more eccentric orbits.

(P3) The integral Δ grows as eccentricities of colliders decrease (see Fig. 5), which may dislodge objects from near-circular orbits.

(P4) Collisional conditions, Eq. (3.31) (gain) and (3.34) (loss). There is a hidden eccentricity dependence here, too. Consider an orbit represented by a certain bin $(e_\star, a_\star)$. This orbit intersects a number of orbits, represented by other (e, a) bins. For larger $e_\star$ the number of such orbits is higher (Fig. B.1). Thus a particle in a more eccentric orbit collides with others more frequently, meaning that we can expect an enhanced depletion of regions with higher eccentricities.

We now describe a series of numerical tests we have undertaken to find out which of these factors actually lead to the effect (ii) observed in the simulations (Fig. B.2). In these tests, we sequentially exclude (P1)–(P4) and their combinations. Figure B.2a is a full simulation result with a V-pattern to be explained (the same as the right bottom panel in Fig. 13). Panel (b) depicts the run without collisional gain. Here, (P1) is excluded, but the pattern survives. In panel (c), we additionally excluded (P2) and (P3) by calculating both $\overline{v_{\text{imp}}}$ and Δ with fixed eccentricities of both colliders artificially set to their maximum values of 0.3. Thus only (P4) is at work here. This changes the pattern appreciably and demonstrates that (P4) does contribute to a depletion at higher e.

We now do the opposite and exclude (P4). It is sufficient to consider a system with only one semimajor bin. As orbits with the same value of a cross each other regardless of their eccentricities, any pair of bins in this case corresponds to intersecting orbits, and the effect depicted in Fig. B.1 is automatically eliminated. Panel (d) corresponds to the case when (P1)–(P3) are at work, and still the "1D-version of the V-pattern" is present: the number of objects peaks at $e \sim 0.1$ as in Figs. B.2a and B.2b. Panel (e) excludes collisional gain and therefore corresponds to the case when (P2) and (P3) are at work; the result is similar. Next, panel (f) represents the run in which we additionally used eccentricity-independent $\overline{v_{\text{imp}}}$ and Δ, like in panel (c). Here, none of the factors (P1)–(P4) are included. It is no surprise therefore, that the distribution becomes uniform. Panels (g) and (h) present the same as (f), but with only one quantity, either $\overline{v_{\text{imp}}}$ or Δ, fixed. As expected, (P3) depletes lower e, whereas (P2) depletes higher e. The final test, presented in panel (i), sets both $\overline{v_{\text{imp}}}$ and Δ to constants, like in panels (c) and (f), but here the collisional gain, effect (P1), is turned on again. There is a slight maximum at intermediate values of e, but the absolute black-white difference here is only marginal, see grey scale bar. To summarize, the whole "eccentricity effect," more objects in orbits with intermediate eccentricities, largely comes from the combined influence of (P2)–(P4). To put it shortly, the effect is explained in terms of collisional probabilities between objects in orbits with different eccentricities.

References

Arakawa, M., 1999. Collisional disruption of ice by high-velocity impact. Icarus 142, 34–45.

Benz, W., Asphaug, E., 1999. Catastrophic disruptions revisited. Icarus 142, 5–20.

Boltzmann, L., 1896. Vorlesungen über Gastheorie. Barth, Leipzig.

Burns, J.A., Lamy, P.L., Soter, S., 1979. Radiation forces on small particles in the Solar System. Icarus 40, 1–48.

Campo Bagatin, A., Cellino, A., Davis, D.R., Farinella, P., Paolicchi, P., 1994. Wavy size distributions for collisional systems with a small-size cutoff. Planet. Space Sci. 42, 1079–1092.

Chandrasekhar, S., 1943. Stochastic problems in physics and astronomy. Rev. Mod. Phys. 15, 1–89.

Chapman, S., Cowling, T.G., 1970. The Mathematical Theory of Nonuniform Gases. Cambridge Univ. Press, New York.

Charnoz, S., Brahic, A., 2001. Long-term collisional evolution of a dissipative particle disc perturbed by a giant-planet embryo. Astron. Astrophys. 375, L31–L34.

Charnoz, S., Thébault, P., Brahic, A., 2001. Short-term collisional evolution of a disc perturbed by a giant-planet embryo. Astron. Astrophys. 373, 683–701.

Davis, D.R., Farinella, P., 1997. Collisional evolution of Edgeworth–Kuiper belt objects. Icarus 125, 50–60.

Davis, D.R., Chapman, C.R., Weidenschilling, S.J., Greenberg, R., 1985. Collisional history of asteroids—evidence from Vesta and the Hirayama families. Icarus 62, 30–53.

Dohnanyi, J.S., 1969. Collisional model of asteroids and their debris. J. Geophys. Res. 74, 2531–2554.

Dominik, C., Decin, G., 2003. Age dependence of the Vega phenomenon: theory. Astrophys. J. 598, 626–635.

Dorschner, J., 1970. Theoretische Untersuchungen über den interstellaren Staub. III. Stauberzeugung durch zirkumstellare Zertrümmerungsprozesse. Astron. Nachr. 292, 79–85.

Durda, D.D., Dermott, S.F., 1997. The collision evolution of the asteroid belt and its contribution to the zodiacal cloud. Icarus 130, 140–164.

Durda, D.D., Stern, S.A., 2000. Collision rates in the present-day Kuiper belt and Centaur regions: applications to surface activation and modification on comets, Kuiper belt objects, Centaurs, and Pluto–Charon. Icarus 145, 220–229.

Durda, D.D., Greenberg, R.R., Jedicke, R., 1998. Collisional models and scaling laws: a new interpretation of the shape of the main-belt asteroid size distribution. Icarus 135, 431–440.

Frezzotti, A., 2001. DSMC simulation of the vertical structure of planetary rings. Astron. Astrophys. 380, 761–775.

Fujiwara, A., Tsukamoto, A., 1980. Experimental study on the velocity of fragments in collisional breakup. Icarus 44, 142–153.

Goldreich, P., Lithwick, Y., Sari, R., 2004. Planet formation by coagulation: a focus on Uranus and Neptune. Annu. Rev. Astron. Astrophys. 42, 549–601.

Greenberg, R., Wacker, J.F., Hartmann, W.K., Chapman, C.R., 1978. Planetesimals to planets: numerical simulation of collisional evolution. Icarus 35, 1–26.

Greenberg, R., Bottke, W.F., Carusi, A., Valsecchi, G.B., 1991. Planetary accretion rates: analytical derivation. Icarus 94, 98–111.

Haug, U., 1958. Über die Häufigkeitsverteilung der Bahnelemente bei den interplanetaren Staubteilchen. Z. Astrophys. 44, 71–97.

Holsapple, K.A., 1994. Catastrophic disruptions and cratering of Solar System bodies: a review and new results. Planet. Space Sci. 42, 1067–1078.

Ida, S., Makino, J., 1993. Scattering of planetesimals by a protoplanet: slowing down of runaway growth. Icarus 106, 210–227.

Kenyon, S.J., Bromley, B.C., 2002. Collisional cascades in planetesimal disks. I. Stellar flybys. Astron. J. 123, 1757–1775.

Kenyon, S.J., Bromley, B.C., 2004a. Collisional cascades in planetesimal disks. II. Embedded planets. Astron. J. 127, 513–530.

Kenyon, S.J., Bromley, B.C., 2004b. The size distribution of Kuiper belt objects. Astron. J. 128, 1916–1926.

Kenyon, S.J., Luu, J.X., 1998. Accretion in the early Kuiper belt. I. Coagulation and velocity evolution. Astron. J. 115, 2136–2160.

Kenyon, S.J., Luu, J.X., 1999a. Accretion in the early Kuiper belt. II. Fragmentation. Astron. J. 118, 1101–1119.

Kenyon, S.J., Luu, J.X., 1999b. Accretion in the early outer Solar System. Astrophys. J. 526, 465–470.

Kholshevnikov, K.V., Shor, V.A., 1994. Velocity distribution of meteoroids colliding with planets and satellites. I. Theory. Astron. Astrophys. Trans. 5, 233–241.

Kley, W., 1999. Mass flow and accretion through gaps in accretion discs. Mon. Not. R. Astron. Soc. 303, 696–710.

Kokubo, I., Ida, S., 1998. Oligarchic growth of protoplanets. Icarus 131, 171–178.

Krivov, A.V., Mann, I., Krivova, N.A., 2000. Size distributions of dust in circumstellar debris disks. Astron. Astrophys. 362, 1127–1137.

Lecavelier des Etangs, A., Scholl, H., Roques, F., Sicardy, B., Vidal-Madjar, A., 1996. Perturbations of a planet on the β Pictoris circumstellar dust disk. 3. Time scale of collisional destruction versus resonance time scale. Icarus 123, 168–179.

Levison, H.F., Morbidelli, A., 2003. The formation of the Kuiper belt by the outward transport of bodies during Neptune's migration. Nature 426, 419–421.

Lissauer, J.J., 1993. Planet formation. Annu. Rev. Astron. Astrophys. 31, 129–174.

Lissauer, J.J., Stewart, G.R., 1993. Planetary accretion in circumstellar disks. In: Phillips, J.A., Thorsett, J.E., Kulkarni, S.R. (Eds.), Planets Around Pulsars. In: ASP Conf. Series, vol. 36. ASP, San Francisco, pp. 217–233.

Lynden-Bell, D., Pringle, J.E., 1974. The evolution of viscous discs and the origin of the nebular variables. Mon. Not. R. Astron. Soc. 168, 603–637.

Monaghan, J.J., 1992. Smoothed particle hydrodynamics. Annu. Rev. Astron. Astrophys. 30, 543–574.

Nakagawa, Y., Hayashi, C., Nakazawa, K., 1983. Accumulation of planetesimals in the solar nebula. Icarus 54, 361–376.

Oort, J.H., van de Hulst, H.C., 1946. Gas and smoke in interstellar space. Bull. Astron. Inst. Netherl. 10, 187–204.

Pan, M., Sari, R., 2004. Shaping the Kuiper belt size spectrum by shattering large but strengthless bodies. Icarus. astro-ph/0402138. In press.

Paolicchi, P., Verlicchi, A., Cellino, A., 1996. An improved semi-empirical model of catastrophic impact processes. I. Theory and laboratory experiments. Icarus 121, 126–157.

Pringle, J.E., 1981. Accretion discs in astrophysics. Annu. Rev. Astron. Astrophys. 19, 137–162.

Résibois, P., de Leener, M., 1977. Classical Kinetic Theory of Fluids. Wiley, New York.

Safronov, V.S., 1969. Evolution of the Protoplanetary Cloud and Formation of the Earth and Planets. Nauka, Moscow. In Russian. English translation: NASA TTF-677, 1972.

Silk, J., Takahashi, T., 1979. A statistical model for the initial stellar mass function. Astrophys. J. 229, 242–256.

Smoluchowski, M.V., 1916. Drei Vorträge über Diffusion, brownsche Bewegung und Koagulation von Kolloidteilchen. Z. Phys. 17, 557–585.

Spahn, F., Albers, N., Sremčević, M., Thornton, C., 2004. Kinetic description of coagulation and fragmentation in dilute granular particle ensembles. Europhys. Lett. 67, 545–551.

Spaute, D., Weidenschilling, S.J., Davis, D.R., Marzari, F., 1991. Accretional evolution of a planetesimal swarm. I. A new simulation. Icarus 92, 147–164.

Sremčević, M., Spahn, F., Duschl, W., 2002. Density structures in perturbed thin cold discs. Mon. Not. R. Astron. Soc. 337, 1139–1152.

Stern, S.A., 1995. Collisional time scales in the Kuiper disk and their implications. Astron. J. 110, 856–868.

Stern, S.A., 1996. Signatures of collisions in the Kuiper disk. Astron. Astrophys. 310, 999–1010.

Stern, S.A., Colwell, J.E., 1997. Collisional erosion in the primordial Edgeworth–Kuiper belt and the generation of the 30–50 AU Kuiper gap. Astrophys. J. 490, 879–882.

Stewart, G.R., Ida, S., 2000. Velocity evolution of planetesimals: unified analytical formulas and comparisons with N-body simulations. Icarus 143, 28–44.

Tanaka, H., Nakazawa, K., 1994. Validity of the statistical coagulation equation and runaway growth of protoplanets. Icarus 107, 404–412.

Thébault, P., Doressoundiram, A., 2003. Colors and collision rates within the Kuiper belt: problems with the collisional resurfacing scenario. Icarus 162, 27–37.

Thébault, P., Augereau, J.C., Beust, H., 2003. Dust production from collisions in extrasolar planetary systems. The inner β Pictoris disc. Astron. Astrophys. 408, 775–788.

Weidenschilling, S.J., Spaute, D., Davis, D.R., Marzari, F., Ohtsuki, K., 1997. Accretional evolution of a planetesimal swarm. 2. The terrestrial zone. Icarus 128, 429–455.

Wetherill, G.W., 1990. Comparison of analytical and physical modeling of planetesimal accumulation. Icarus 88, 336–354.

Wetherill, G.W., Stewart, G.R., 1989. Accumulation of a swarm of small planetesimals. Icarus 77, 350–357.

Wetherill, G.W., Stewart, G.R., 1993. Formation of planetary embryos: effects of fragmentation, low relative velocity, and independent variation of eccentricity and inclination. Icarus 106, 190–209.